International Journal of Robotics and Control Systems
Vol. 5, No. 6, 2025, pp. 3015-3046
ISSN 2775-2658
http://pubs2.ascee.org/index.php/ijrcs

High-Performance ANN-SMC MPPT Control with Adaptive Super-Twisting Observer for Enhanced Stability in Grid-Connected PV Systems

Le Duc Hao [a,1], Le Van Dai [a,2,*]

[a] Electric Power System Research Group, Faculty of Electrical Engineering Technology, Industrial University of Ho Chi Minh City, Ho Chi Minh City, Vietnam
[1] 23742351.hao@student.iuh.edu.vn; [2] levandai@iuh.edu.vn
* Corresponding Author

ARTICLE INFO

Article history
Received October 16, 2025
Revised November 16, 2025
Accepted December 15, 2025

Keywords
Artificial Neural Networks;
Adaptive Super Twist Observer;
Sliding Mode Control;
DC-link Stability;
Photovoltaic System

ABSTRACT

Grid-connected photovoltaic (PV) systems face significant stability challenges due to rapid irradiance fluctuations and severe grid faults. Conventional maximum power point tracking (MPPT) algorithms often struggle with slow convergence and oscillations under these conditions. This study aims to improve system stability, dynamic performance, and power quality through a novel adaptive hybrid control strategy. The proposed controller integrates an artificial neural network (ANN) for precise reference voltage generation with sliding mode control (SMC), enhanced by an adaptive super-twisting observer (ASTO). This combination effectively estimates unmeasured states and mitigates chattering phenomena. The system is validated using MATLAB/Simulink under rapidly changing solar irradiance and both symmetrical and asymmetrical fault scenarios. Simulation results show that the proposed method significantly reduces DC-link voltage overshoot and settling time compared to conventional methods, ensuring fast and stable tracking. The method achieves a superior total harmonic distortion (THD) of 1.34% and maintains robust operation during faults. The novelty of this approach lies in the ASTO-based ANN-SMC framework, which ensures robust tracking under severe nonlinear disturbances. This solution provides a resilient method to enhance energy conversion efficiency in modern grid-integrated renewable systems.

1. Introduction

Renewable energy sources [1], particularly solar power [2], have emerged as a pivotal solution in the global transition toward sustainable energy systems. Their environmentally benign nature and virtually inexhaustible availability make them ideal substitutes for conventional fossil fuels [3]-[7]. In parallel, the development of advanced motor control technologies plays a crucial role in optimizing [8] energy conversion efficiency, ensuring system stability, and enhancing the overall performance of renewable energy applications [9]-[11]. Among the renewable energy sources, photovoltaic (PV) systems are widely deployed in many countries in both grid-connected and standalone forms, serving a variety of applications in energy production and industrial sectors [12]-[15]. However, the energy

conversion efficiency of PV systems is strongly influenced by environmental conditions such as shading, dust, temperature, and radiation intensity, which in turn affect the determination of the maximum power point (MPP) [16]-[19].

Tracking and maintaining the MPP, also known as MPP tracking (MPPT), is a key factor in ensuring optimal energy extraction from the PV system. Traditional algorithms, such as perturb and observe (P&O) and incremental conductance [20], although advantageous in terms of simple structure and ease of implementation, face challenges under rapidly changing weather conditions due to large fluctuations and relatively low accuracy [21]-[24]. Furthermore, grid-connected PV systems typically include PV panels, DC-DC converters [25], DC-AC inverters, MPPT controllers, and grid connection controllers [26]-[30]. However, when grid faults such as voltage sags occur, particularly severe faults like three-phase to ground short circuits, the grid voltage can drop sharply over a short period, causing instability in the PV system and forcing the inverter to disconnect from the grid [28], [31]-[33]. While renewable energy system design has advanced, ensuring stability, control capability, and high performance remains a major challenge due to the complex operational and control characteristics [2], [21], [22], [34], [35]. Enhancing the stability of renewable energy systems through control methods is a rapidly growing area of research. Among these, PV systems have been widely deployed across many countries [12], [36], [37]. PV systems are generally categorized into two main types based on their intended use. The first category is grid-connected PV systems, including hybrid systems, power plants, grid-connected systems, and other integrated applications. The second category is standalone PV systems, which are used to power devices such as electric vehicles, pumps, streetlights, space applications, and other self-operating equipment [12], [38]-[40]. To maximize the power output of PV systems under varying radiation and temperature conditions, MPPT methods have been integrated [4], [41].

In recent years, various improvements to conventional MPPT algorithms have been proposed to enhance tracking accuracy and reduce power loss under rapidly changing environmental conditions. For example, Killi and Samanta [42] modified the classical P&O algorithm by incorporating the current variation ΔI alongside ΔP and ΔV to mitigate the drift phenomenon that occurs when irradiance changes suddenly and modified the classical P&O algorithm by incorporating the current variation ΔI alongside ΔP and ΔV to mitigate the drift phenomenon that occurs when irradiance changes suddenly. This approach improved the dynamic tracking capability and reduced energy losses, but its heuristic nature limited adaptability under complex fault scenarios. Similarly, Shang et al. [43] enhanced the Incremental Conductance method by analyzing instantaneous variations in current, voltage, and power to accelerate convergence and minimize oscillations. Although this method achieved a 20-30% improvement in tracking speed compared with the traditional IncCond, it still lacked self-learning capability and robustness against grid disturbances. To address issues related to partial shading and multiple local maxima, several hybrids or metaheuristic-based MPPT methods have been introduced. Abo-Khalil et al. [44] combined simulated Annealing with the P&O method, using SA to approximate the GMPP and P&O for fine-tuning, resulting in reduced oscillations and shorter convergence time. However, the increased computational complexity limited its suitability for real-time applications; similarly, Xiao et al. [45] proposed a hybrid slime mold-golden sine algorithm for GMPP tracking, demonstrating superior convergence and accuracy on benchmark tests compared to PSO and TSO. Yet, the heavy computational demand and lack of fault-tolerant assessment restrict its deployment in grid-connected systems. In another approach, Harrag and Messalti [46], optimized the step size of P&O using a Genetic Algorithm to balance speed and stability during tracking. Although the GA-P&O achieved flexible step adaptation and improved dynamic response, it relied on offline optimization and did not explicitly address system behavior under severe grid faults.

Overall, while these studies have successfully improved MPPT efficiency under varying irradiance or shading, they remain predominantly heuristic and lack adaptability to unpredictable fault conditions such as three-phase fault to ground (LLLG). Moreover, none of these methods explicitly evaluates DC-link voltage overshoot, total harmonic distortion (THD) reduction, fault ride-through capability, key indicators of grid-connected PV stability. These limitations underscore the need for an intelligent control strategy that can learn nonlinear relationships, adapt to real-time disturbances, and

facilitate faster recovery during faults. Consequently, the integration of an artificial neural network (ANN) trained by the levenberg-marquardt (LM) algorithm [47] emerges as a promising approach to enhance MPPT performance, reduce transient oscillations, and improve overall system stability under both dynamic environmental changes and grid fault conditions. Therefore, machine learning techniques, particularly ANNs, have been applied to the MPPT problem. ANN can model the nonlinear relationship between inputs such as voltage, current, temperature, and output power without the need for prior assumptions about the mathematical model. In this study, the application of ANN for MPPT is designed with an input dataset consisting of historical values of voltage V_{pv} and current I_{pv} to estimate the duty cycle, thereby optimizing the output power of the DC/DC converter [25]. Unlike traditional ANN methods based on popular training algorithms such as Backpropagation or Gradient Descent, this study combines ANN and SMC, a powerful and efficient technique, to improve the neural network training process for MPPT optimization. SMC allows for fast convergence with minimal error, which is especially suitable for nonlinear regression models such as the multilayer perceptron. Therefore, ANN combined with SMC not only significantly improves the accuracy of power prediction but also ensures high stability and adaptability under rapidly changing weather conditions. In addition, the adaptive super-twisting observer (ASTO) is an advanced state observation method belonging to the Sliding mode observer family, which is specially designed for nonlinear systems tolerant to disturbances and uncertainties. The outstanding advantage of ASTO lies in its ability to significantly reduce chattering and ensure fast convergence, which helps to accurately estimate state variables that cannot be measured directly. In addition, the adaptive mechanism allows the observer to maintain high stability and robustness even when operating conditions change continuously. The main goal of this method is to design an intelligent MPPT controller using an ANN combined with SMC with ASTO, which is capable of fast and stable MPPT positioning while minimizing power fluctuations and energy losses. This method is verified through simulations involving scenarios with changes in radiation and temperature, evaluating performance based on response time, stability, power quality, and energy yield [48], [49].

The primary objective of this study is to design a novel adaptive hybrid MPPT controller to enhance stability, dynamic performance, and power quality under both environmental changes and severe grid faults. The specific contributions are:

1. Developing an MPPT controller using ANN combined with SMC and ASTO for accurate system identification and dynamic control.
2. Evaluating the controller's robustness against DC-link overvoltage and THD under severe grid faults.
3. Demonstrating the superiority of the proposed method over conventional techniques in terms of stability and power quality

The remainder of the paper is organized as follows: Section 2 focuses on the grid-connected solar power conversion system, analyzing the theoretical basis of the PV array model. Section 3 discusses the proposed control solutions for MPPT, including the conventional control solution and the proposed control solution. Section 4 presents the results and simulations of the study, in which the system is tested in both scenarios. Finally, the conclusion summarizes the main findings of the study.

2. Photovoltaic Power Conversion System Interfaced with the Grid

In Fig. 1, a grid-connected PV system, consisting of two arrays, is studied, which is modeled and simulated at standard conditions of 1000 W/m^2, cell temperature of 25°C corresponding to each array having a capacity of 219.961 W. A DC-DC boost converter is connected to each variety, where an MPPT control algorithm based on an ANN is implemented to maximize the efficiency from the PV arrays by adjusting the respective terminal voltages. A 1000 V-rated voltage is connected from the power converters to a common DC bus, which remains constant regardless of changes in the input power of each PV array. The generation of 500 V is achieved through a three-level neutral point clamped inverter to convert the energy to three-phase AC. Reactive power up to ±1 MVAr is achieved

thanks to the system being supplemented with a reactive power controller that allows the desired power to be consumed or emitted. A three-phase transformer with a rated capacity of 2.25 MVA and a rated voltage of 500 V/25 kV is the bridge to connect the grid and the PV system. The grid-side model includes a 25 kV distribution line and a 120 kV transmission grid.

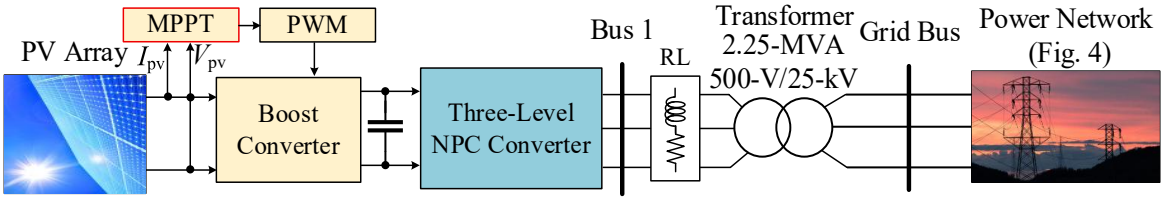

Fig. 1. Solar energy system connected to the utility grid

2.1. Model of the Photovoltaic Array

The equivalent circuit model represents [50], the overall *I-V* characteristic of a PV cell, module, or array is through a continuous mathematical relationship involving key electrical variables. The diode equivalent circuit model is commonly used to represent the electrical behavior of a PV cell. A PV array is formed by connecting multiple PV modules in series to achieve the desired voltage and in parallel to provide the required current. This configuration allows the system to efficiently meet specific power requirements, as illustrated in Fig. 2 [51]-[55].

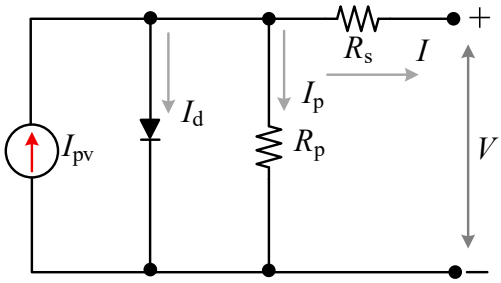

Fig. 2. Equivalent circuit of a PV cell

To mathematically describe the equivalent circuit of a PV cell, Kirchhoff's current law is applied, leading to the following expression for the output current [50], [56], [57]:

$$I = I_{pv} - I_d - I_p \tag{1}$$

where I_{pv} is the photocurrent, I_d is the loss diode current, and I_p is the shunt current. The diode current I_d in a single-diode PV model follows the Shockley equation for an ideal diode [58]:

$$I_d = I_s[exp(\frac{(V + R_s I)q}{n(\frac{(kT_c)}{q})}) - 1] \tag{2}$$

where I_s is the reverse saturation current of the diode, q is the electron charge (1.6×10^{-19}C), n is the diode ideality factor typically between 1 and 2, R_s is the internal series resistance, V is the terminal voltage of the PV cell, k is the Boltzmann's constant (1.38×10^{-23} J/K), and T_c is the cell's junction temperature in Kelvin [59]. Meanwhile, the shunt current I_p, caused by leakage through the shunt resistance R_p, is given by:

$$I_p = \frac{(V + R_s I)q}{R_p} \tag{3}$$

Combining these relationships, the final expression for the output current of the single-diode PV model is:

$$I = I_{\text{pv}} - I_{\text{s}}[\exp((\frac{(V + R_{\text{s}}I)q}{n(\frac{(kT_{\text{c}})}{q})}) - 1)] - (\frac{(V + R_{\text{s}}I)q}{R_{\text{p}}}) \quad (4)$$

This comprehensive formulation captures both the diode's nonlinear characteristics and the effects of resistive losses within the PV cell. The simulation and demonstration are based on a Solarex PV module, Canadian Solar Inc. CS5P-220M, consisting of 66 polycrystalline cells connected in a datasheet of PV arrays used [60]. The *I-V* and *P-V* characteristics of the *PV* array are illustrated in Fig. 3 (a) and (b).

The operational features of a solar PV system, especially its *P-V* and *I-V* curves, are greatly affected by the current environmental conditions, as shown in the referenced figure. Understanding these curves is key to evaluating the power output of the PV system under different scenarios. The MPP on these curves, which indicates where the system delivers its highest power, varies with changes in temperature and sunlight intensity. To precisely identify the MPP based on the existing environmental factors, an artificial neural network (NN) is used. This technique draws on the NN's capability to process non-linear connections and complex patterns, making it well-suited for forecasting the MPP from inputs such as temperature and solar radiation levels [61].

2.2. Modeling of Key Components in Grid-Connected Systems

The model in Fig. 4 represents a complete three-phase power network, integrating essential components such as high-voltage sources, step-down transformers, transmission lines, and parallel RLC loads. In this configuration, the transformer steps down the voltage from 120 kV to 25 kV and has a rated capacity of 47 MVA, allowing for power transfer between different voltage levels. The three-phase source provides the system with a voltage of 120 kV and a short-circuit capacity of 2500 MVA, ensuring a robust and stable input power supply. An earthing transformer is integrated to protect the system under fault conditions and enhance operational safety. The transmission section consists of three lines with lengths of 8 km, 2 km, and 6 km, respectively, allowing for the representation of distributed electrical properties such as resistance, inductance, and capacitance. Two parallel RLC loads rated at 30 MW and 2 MW simulate real-world power consumption, supporting the analysis of how different load levels affect dynamic behavior and voltage stability. Voltage and current sensors placed at key points enhance monitoring capabilities, allowing for early fault detection and performance evaluation. Overall, the model is a useful tool for assessing the stability and performance of grid-connected PV systems.

3. Advanced Strategy for Maximum Power Point Tracking in PV Systems

3.1. Perturb and Observe Algorithm

The perturb and observe (P&O) algorithm MPPT, or the conventional method algorithm, provides a simple and efficient method for tracking the MPPT of a PV system, while ensuring originality. The MPPT determines the point at which the PV system produces its maximum power. The algorithm starts by initializing the operating point of the PV system at a random value. Then, the algorithm adjusts the operating point slightly. Next, the algorithm measures the subsequent change in the output power. If the output power increases suddenly, the algorithm moves in the direction of adjustment. Conversely, if the output power decreases, the algorithm moves in the opposite direction to the initial adjustment. The P&O algorithm works by periodically adjusting the PV system operating point and evaluating subsequent changes in output power. The algorithm systematically progresses towards increasing output power until the MPP is reached, the block diagram of which is shown in Fig. 5 [62]-[66].

Finally, after each adjustment, the values of $D(t)$, $V_{\text{pv}}(t)$, $I_{\text{pv}}(t)$, and $P_{\text{pv}}(t)$ are stored and used in subsequent iterations, enabling the system to continue tracking the MPP stably. However, synchronization with the MPPT can be slow, especially in cases where the MPPT experiences rapid

fluctuations. The convergence speed of the P&O algorithm is correlated with the adjustment amplitude. Larger adjustments increase the convergence speed but also increase the risk of overshooting the MPP. Therefore, it is important to apply a more improved method to solve these problems. Therefore, the proposed method is presented in the next section.

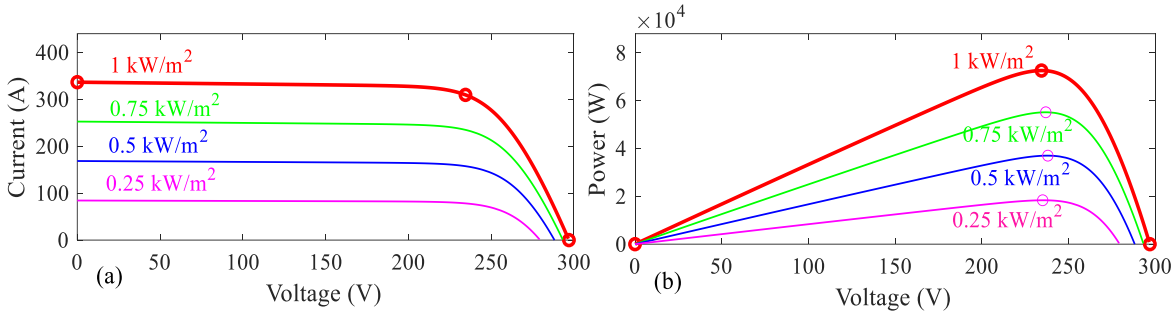

Fig. 3. Specifications of a PV array at 25ºC of an array type of Canadian Solar Inc. CS5p-220N; 5 series modules; 66 parallel strings; (a) the *I-V* characteristic and (b) the *P-V* characteristic

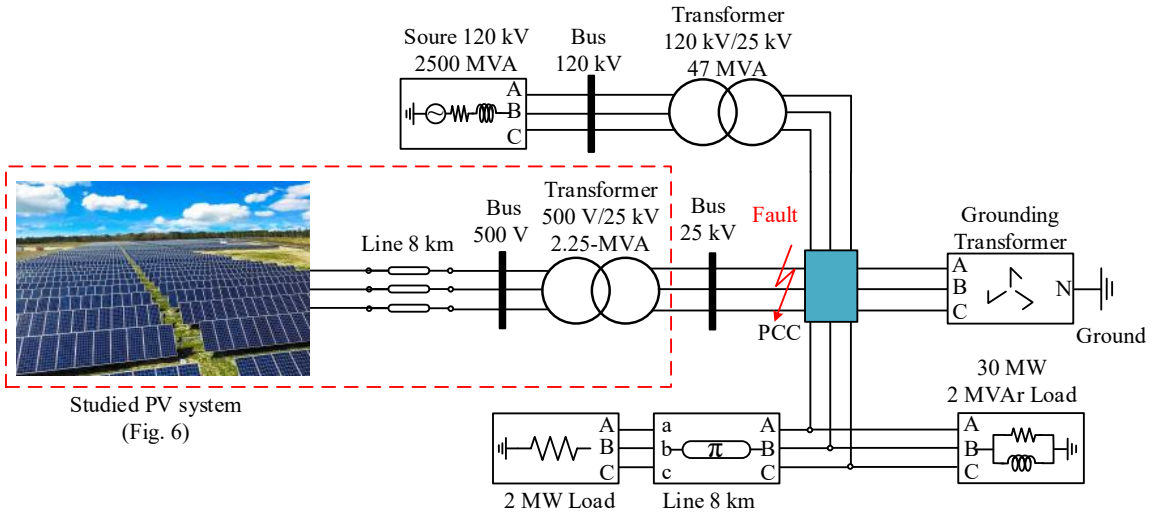

Fig. 4. The system represents a three-phase power network

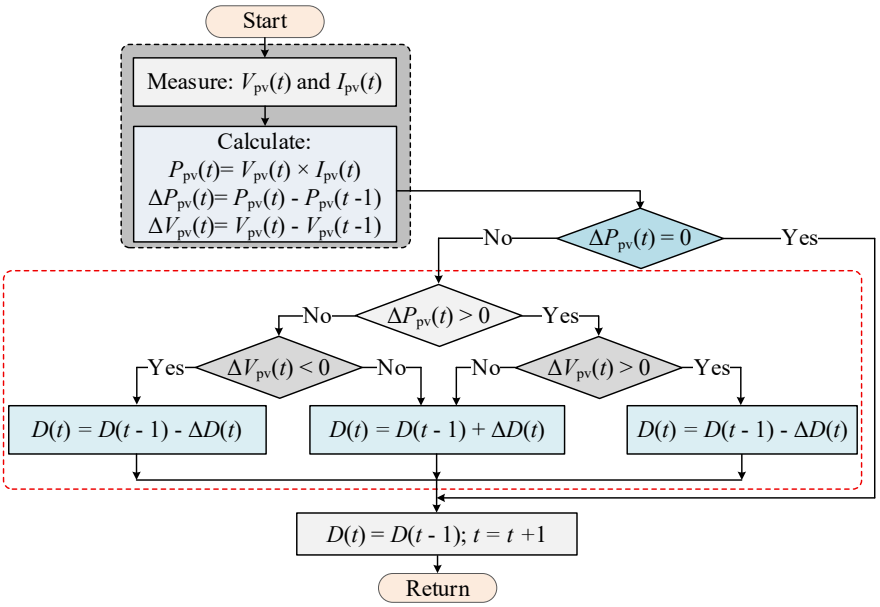

Fig. 5. Flowchart of the P&O-MPPT algorithm using the dynamic step size tuning solution

3.2. Proposed Method MPPT

The PV system under study is fully illustrated in Fig. 1, which includes all the basic components of the panels and the boost converter used in this study. The boost converter operates to regulate the voltage and current between the panels and the grid, thereby maximizing the power transmission efficiency. In terms of control, the conventional system is divided into two main blocks: boost converter control and inverter control.

The inverter control controls the DC-AC voltage source and is built on a combination of a power balance controller and a PI controller that provides feedback on the DC link voltage. In addition, it integrates a converter module that performs essential functions such as phase-locked loop (PLL) and *dq* coordinate transformation to control the current in the rotating synchronous coordinate system shown in Fig. 6. Together with the converter, the algorithm combines ANN and sliding mode control to observe MPPT using advanced computational techniques to actively maintain the optimal power operating point of the PV system.

To ensure optimal power extraction under changing real-world environmental conditions and source/load fluctuations, ASTO is proposed. In this application, ASTO is responsible for estimating the necessary inputs to the SMC controller. Specifically, ASTO estimates the induced current and applied output of the system, providing important data for the MPPT controller to decide. The following subsections will focus on the detailed modeling analysis of this intelligent hybrid controller and the design of the ASTO tool [67]-[69].

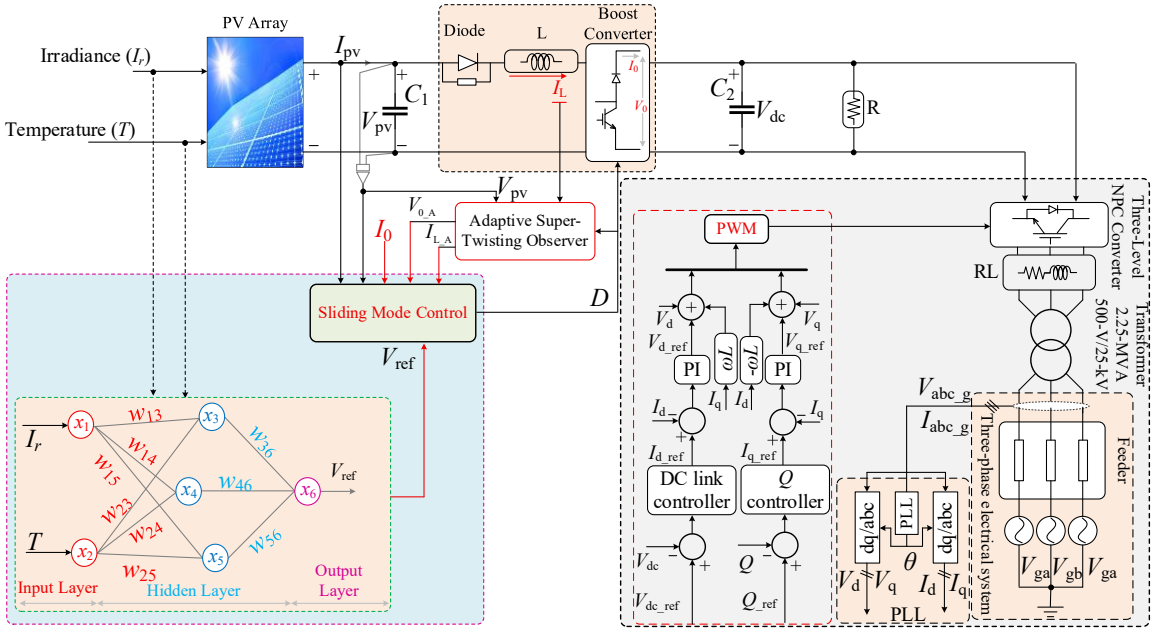

Fig. 6. Proposed MPPT control method diagram for PV system

Temperature and irradiance are fed into the ANN controller through three steps, including the input layer, the hidden layer, and the output layer, to determine the reference voltage Vref corresponding to the maximum power operating point. The generated reference voltage is then forwarded to the SMC controller, combined with ASTO, which estimates the input/state for the SMC controller, which in turn adjusts the converter to ensure the PV system continuously tracks the MPPT. The MPPT at any operating condition can be efficiently determined using the sliding mode formula to generate the desired reference voltage. This is done by defining a suitable sliding surface to adjust the convergence of the operating point towards the maximum power condition, as shown in Fig. 6.

3.2.1. Adaptive Super-Twisting Observer

To design the ASTO, we consider the dynamic analytical relationship of the induced current and capacitor voltage in the boost converter [70].

$$\begin{cases} \dfrac{\mathrm{d}I_{\mathrm{L}}}{\mathrm{d}t} = \dfrac{V_{\mathrm{pv}} - ((1-D)V_0)}{L} \\ \dfrac{\mathrm{d}V_0}{\mathrm{d}t} = \dfrac{(1-D)I_{\mathrm{L}}}{L} + \dfrac{V_0}{RC_2} \end{cases} \tag{5}$$

where V_0 is the output voltage in the boost converter, C_2 is the output capacitor, R is the resistance load, and L is the inductance. Therefore, the ASTO method is presented as follows:

$$\hat{I}_{\mathrm{L\_A}} = \frac{\mathrm{d}\hat{I}_{\mathrm{L}}}{\mathrm{d}t} = \frac{1}{L}\left[-(1-D)\hat{V}_0 + V_{\mathrm{pv}}\right] + \left[\frac{\hat{\alpha}_1}{L}|e_{\mathrm{L}}|^{\frac{1}{2}}\mathrm{sign}(e_{\mathrm{L}}) + \hat{\alpha}_2\int \mathrm{sign}(e_{\mathrm{L}})\mathrm{d}t + n_0 e_{\mathrm{L}}\right] \tag{6}$$

$$\hat{V}_{0\_\mathrm{A}} = \frac{\mathrm{d}\hat{V}_0}{\mathrm{d}t} = \frac{1}{C_2}\left[(1-D)\hat{I}_{\mathrm{L}} + \frac{1}{R}\hat{V}_0\right] - \sigma_1\hat{\alpha}_1|e_{\mathrm{L}}|^{\frac{1}{2}}\mathrm{sign}(e_{\mathrm{L}}) - \sigma_1\hat{\alpha}_2\int \mathrm{sign}(e_{\mathrm{L}})\mathrm{d}t - n_0 e_{\mathrm{L}} \tag{7}$$

To smooth the signal and accelerate convergence, a linear component has been introduced, and the two gain coefficients have been synchronized in ASTO. Since the super-twisted observer essentially involves non-linear equations due to the presence of sign functions and two gain coefficients. Therefore, this study defines the nonlinear component as $n_0 e_{\mathrm{L}}$, where n_0 is the positive gain coefficient, and the adaptive dynamic gain coefficients α_1 and α_2 are expressed as follows [70]-[72]:

$$\begin{cases} e_{\mathrm{L}} = \hat{I}_{\mathrm{L}} - I_{\mathrm{L}} \\ \dfrac{\mathrm{d}\hat{\alpha}_1}{\mathrm{d}t} = \beta\left(-\dfrac{1-D}{L}\dfrac{\mathrm{d}e_{V_0}}{\mathrm{d}t} - n_0\dfrac{\mathrm{d}e_{\mathrm{L}}}{\mathrm{d}t}\right)|e_{\mathrm{L}}|^{\frac{1}{2}} \qquad (\beta < -1) \\ \dfrac{\mathrm{d}\hat{\alpha}_2}{\mathrm{d}t} = \dfrac{\mathrm{d}\hat{\alpha}_1}{\mathrm{d}t}\varepsilon \\ \varepsilon < \sqrt{\left|\left(-\dfrac{1-D}{L}\dfrac{\mathrm{d}e_{V_0}}{\mathrm{d}t} - n_0\dfrac{\mathrm{d}e_{\mathrm{L}}}{\mathrm{d}t}\right)|e_{\mathrm{L}}|^{\frac{1}{2}}\right|(1-\beta) + \dfrac{\frac{\mathrm{d}\hat{\alpha}_1}{\mathrm{d}t}}{2}} \end{cases} \tag{8}$$

In with ε is the parameter of ASTO to satisfy Eq. (8). The error in estimating the induced current is defined by the first derivative equation as follows:

$$\frac{\mathrm{d}e_{\mathrm{L}}}{\mathrm{d}t} = \frac{\mathrm{d}\hat{I}_{\mathrm{L}}}{\mathrm{d}t} - \frac{\mathrm{d}I_{\mathrm{L}}}{\mathrm{d}t} \tag{9}$$

Substituting the current equation in Eq. (5) into Eq. (6) and Eq. (9), we can rewrite it as follows:

$$\begin{aligned} \frac{\mathrm{d}e_{\mathrm{L}}}{\mathrm{d}t} &= \left(\frac{1}{L}\left[-(1-D)\hat{V}_0 + V_{\mathrm{pv}}\right] + \frac{\hat{\alpha}_1}{L}|e_{\mathrm{L}}|^{\frac{1}{2}}\mathrm{sign}(e_{\mathrm{L}}) + \hat{\alpha}_2\int \mathrm{sign}\,(e_{\mathrm{L}})\mathrm{d}t + n_0 e_{\mathrm{L}}\right) - \left(\frac{V_{pv} - (1-D)V_0}{L}\right) \\ &= \frac{1-D}{L}(V_0 - \hat{V}_0) + \left[\frac{\hat{\alpha}_1}{L}|e_{\mathrm{L}}|^{\frac{1}{2}}\mathrm{sign}(e_{\mathrm{L}}) + \hat{\alpha}_2\int \mathrm{sign}\,(e_{\mathrm{L}})\mathrm{d}t + n_0 e_{\mathrm{L}}\right] \end{aligned} \tag{10}$$

where $z(t) = \hat{\alpha}_2\int \mathrm{sign}\,(e_{\mathrm{L}})\mathrm{d}t$, and $w(t) = \frac{1-D}{L}(V_0 - \hat{V}_0)$, let $A_1 = \hat{\alpha}_1/L$. To analyze the stability of the nonlinear, nonsmooth system in Eq. (10), the following assumptions are introduced. The disturbance term $w(t)$ is bounded, i.e., there exists $W \geq 0$ such that $|w(t)| \leq W, \forall t$. The integral term $z(t)$ is bounded in the region of interest. That is, there exists $Z \geq 0$ such that the sign of the nonlinear coefficient is known. Two important cases arise: if $A_1 < 0$, where the nonlinear term contributes to dissipation; if $A_1 > 0$, where the nonlinear term may destabilize the system. The linear gain n_0 satisfies $n_0 \leq 0$, or is sufficiently small positive such that local dominance of the negative nonlinear term is preserved. To stabilize the system, we consider the Lyapunov function as follows.

$$V(e_{\mathrm{L}}) = \frac{1}{2}e_{\mathrm{L}}^2 \tag{11}$$

For $e_L \neq 0$, its derivative along trajectories of Eq. (10) as follows:

$$\frac{dV}{dt} = e_L \frac{de_L}{dt} = e_L w(t) + A_1 |e_L|^{\frac{3}{2}} + e_L z(t) + n_0 e_L^2 \quad (12)$$

Using the bounds $|w(t)| \leq W$ and $|z(t)| \leq Z$, we obtain as follows:

$$\frac{dV}{dt} \leq (W + Z)\,|e_L| + A_1 |e_L|^{\frac{3}{2}} + n_0 e_L^2 \quad (13)$$

Express $|e_L| = \sqrt{2V}$, $|\,e_L\,|^{3/2} = (2V)^{3/4}$, and $e_L^2 = 2V$. Substituting into Eq. (13) gives:

$$\frac{dV}{dt} \leq (W + Z)\sqrt{2V} + A_1 W + Z)(\sqrt{2V})^2 + n_0 V \quad (14)$$

Because $A_1 < 0$, the dominant term near the origin is the negative nonlinear component:

$$A_1 (2V)^{\frac{3}{4}} = 0 \quad (15)$$

As $V \to 0$, the terms $\sqrt{V}$ and V become negligible compared to $V^{3/4}$. Hence, there exists $\varepsilon > 0$ such that for all $0 < V < \varepsilon$:

$$\frac{dV}{dt} \leq -c(V)^{\frac{3}{4}} \quad (16)$$

For some constant $c = -\frac{1}{2} A_1 2^{3/4} > 0$. Integrating Eq. (17) yields the classical finite-time convergence inequality:

$$T \leq \frac{4}{c} V(0)^{\frac{1}{4}} < \infty \quad (17)$$

Therefore, $V(t) \to 0$, and consequently $e_L(t) \to 0$, in finite time.

3.2.2. MPPT Control Design-Based ANN-SMC

The proposed MPPT strategy integrates an ANN-based voltage estimator with a sliding-mode control layer, where the ANN predicts the optimal MPP voltage based on irradiance and temperature. Meanwhile, the SM controller utilizes three tracking errors: PV voltage, inductor current, and load voltage to ensure robust convergence toward the estimated MPPT. This hybrid design enhances adaptability to environmental variations while maintaining strong disturbance rejection and stability. To calculate the optimal operating voltage at the MPPT, a feed-forward ANN is used, using illuminance and temperature as input features through the following three basic steps [73].

Step 1. Hidden layer output. First, the net input $n^{(1)}$ to the hidden layer is calculated through an affine transformation of the input vector x_{in}:

$$n^{(1)} = W^{(1)} x_{in} + b^{(1)} \quad (18)$$

The output of the hidden layer h is obtained by applying the nonlinear activation function $\phi(.)$ element-wise to the net input:

$$h = \phi\left(n^{(1)}\right) = \phi\left(W^{(1)} x_{in} + b^{(1)}\right) \quad (19)$$

Step 2. Output layer calculation. The final control reference signal V_{ref}, which is x_6, is calculated based on the linear combination of the hidden layer outputs h and the output layer weights $w^{(2)}$. The net input to the output layer $n^{(2)}$ is:

$$n^{(2)} = w^{(2)T} h + b^{(2)} \quad (20)$$

Finally, the control signal V_{ref} is the result of applying the output activation function $\vartheta(.)$ to $n^{(2)}$:

$$V_{\text{ref}} = x_6 = \vartheta\left(n^{(2)}\right) = \vartheta(w^{(2)T}h + b^{(2)}) \tag{21}$$

By substituting the expression for h into the final output equation, the complete closed-form control signal V_{ref} is:

$$V_{\text{ref}}(x_{\text{in}}, W) = \vartheta(w^{(2)T}(\phi\left(W^{(1)}x_{\text{in}} + b^{(1)}\right)) + b^{(2)}) \tag{22}$$

Once the V_{ref} data is updated into the SMC, we identify three main tracking errors that are used to adjust the MPPT system operation to achieve optimal power tracking. These three errors represent the difference between the measured/estimated system value and the desired reference value expressed through the following equations.

Error 1. Panel voltage error e_1:

$$e_1 = V_{\text{pv}} - V_{\text{ref}} \tag{23}$$

This error measures the difference between the actual panel voltage V_{pv} and the optimal voltage V_{ref}, which is the voltage at the MPP.

Error 2. Panel current error e_2:

$$e_2 = \hat{I}_{\text{L}} - I_{\text{L\_ref}} \tag{24}$$

This error compares the estimated inductor current $\hat{I}_{\text{L}}$ with the inductor current reference $I_{\text{L\_ref}}$. The reference value $I_{\text{L\_ref}}$ is defined as:

$$I_{\text{L\_ref}} = -C_1 V_{\text{pv}} + I_{\text{pv}} \tag{25}$$

where C_1 is a constant related to the panel, often its capacitance, V_{pv} is the panel voltage, and I_{pv} is the panel current. Substituting $I_{\text{L\_ref}}$ into the e_2 expression yields:

$$e_2 = \hat{I}_{\text{L}} - I_{\text{pv}} + C_1 V_{\text{pv}} \tag{26}$$

Error 3. Load voltage error e_3:

$$e_3 = V_{0\_\text{ref}} - \hat{V}_{0\_\text{A}} \tag{27}$$

This error is the difference between the load voltage reference V_{0_ref} and the estimated load voltage $\hat{V}_0$, $\hat{V}_{0\_\text{A}}$ and $\hat{I}_{\text{L_A}}$are estimations of V_0 and I_{L} using an ASTO observer. The load voltage reference V_{0_ref} is defined based on Ohm's law for the load with a purely resistive load R and load current I_0:

$$V_{0\_\text{ref}} = I_0 R \tag{28}$$

Combining the Eqs (28) and (29), it yields the following:

$$e_3 = I_0 R - \hat{V}_{0\_\text{A}} \tag{29}$$

The control law used in this case is a form of SMC, which generates the control signal $u(t)$ to ensure the system tracks the optimal power point. The sliding surface s is a linear weighted combination of the defined tracking errors:

$$s = \sum_{\text{i}=1}^{3} k_{\text{i}} e_{\text{i}} = ke_1 + ke_2 + ke_3 \tag{30}$$

where $k_i > 0$ are the gains selected to ensure the system's stability and convergence. The goal of SMC is to drive the system to reach and stay on the sliding surface, i.e., $s \approx 0$. The control signal $u(t)$ is a sign function of the sliding surface s, multiplied by the gain k_i:

$$u(t) = k_4 \text{sign}(s(t)); \; with \; k4 \; > \; 0 \tag{31}$$

The sign($s(t)$) function generates the switching control signal, which is characteristic of SMC:

$$\text{sign}\big(s(t)\big) = \begin{cases} 1 \\ 0 \\ -1 \end{cases}, \begin{cases} s(t) > 0 \\ s(t) = 0 \\ s(t) < 0 \end{cases} \tag{32}$$

This control law ensures that when the system is off the sliding surface $s \neq 0$, the control signal drives the system back towards the surface $s \to 0$. The gains k_i cannot be chosen arbitrarily; they must satisfy a stability condition to ensure the effective operation of the sliding mode:

$$k_3 = \frac{C_1}{C_0} < k_1 < k_2 \frac{C_1 \frac{\text{d}I_{\text{L\_ref}_{\max}}}{\text{d}t}}{I_{\text{pv\_max}}} \tag{33}$$

where C_{pv} and C_0 are the panel capacitance and the output capacitance, respectively. $I_{\text{L\_ref}_{\max}}$ and $I_{\text{pv\_max}}$ these are the maximum values of the derivative of the inductor's current reference, representing its maximum rate of change. This condition constrains the value of k_1 related to voltage error e_1 between a ratio involving k_3 and k_2, ensuring that the dynamics of the errors are balanced to achieve system stability. To ensure the reliability of the MPPT controller, stability analysis is crucial. The Lyapunov method is employed to prove the system's convergence to the desired state, the sliding surface $s = 0$ [70], [74].

Panel voltage rate of change:

$$\frac{\text{d}V_{\text{pv}}}{\text{d}t} = \frac{1}{C_1}(I_{\text{pv}} - \hat{I}_{\text{L}}) \tag{34}$$

Inductor current rate of change:

$$\frac{\text{d}I_{\text{pv}}}{\text{d}t} = \frac{V_{\text{pv}} - \hat{V}_0 + D\hat{V}_0}{L} \tag{35}$$

Output voltage rate of change:

$$\frac{\text{d}V_0}{\text{d}t} = \frac{1}{C_2}(\frac{\hat{V}_0}{R} + \hat{I}_{\text{L}} - D\hat{I}_{\text{L}}) \tag{36}$$

The convergence of the tracking errors, e_i, demonstrates the stability. We calculate the time derivative of the errors:

$$\begin{cases} \frac{\text{d}e_1}{\text{d}t} = \frac{\text{d}V_{\text{pv}}}{\text{d}t} - \frac{\text{d}V_{\text{ref}}}{\text{d}t} \\ \frac{\text{d}e_2}{\text{d}t} = \frac{\text{d}\hat{I}_{\text{L}}}{\text{d}t} - \frac{\text{d}I_{L\_ref}}{\text{d}t} \\ \frac{\text{d}e_3}{\text{d}t} = \frac{\text{d}V_{0\_\text{ref}}}{\text{d}t} - \frac{\text{d}\hat{V}_{0\_\text{A}}}{\text{d}t} \end{cases} \tag{37}$$

Substituting the boost converter dynamics Eqs. (35)-(37) into the error derivative expressions:

$$\begin{cases} \dfrac{de_1}{dt} = \dfrac{1}{C_1}(I_{pv} - \hat{I}_L) - \dfrac{dV_{ref}}{dt} \\ \dfrac{de_2}{dt} = \dfrac{1}{L}(V_{pv} - \hat{V}_0 + D\hat{V}_0) - \dfrac{dI_{L\_ref}}{dt} \\ \dfrac{de_3}{dt} = \dfrac{dV_{0\_ref}}{dt} - \dfrac{1}{C_2}(\dfrac{\hat{V}_0}{R} + \hat{I}_L - D\hat{I}_L) \end{cases} \tag{38}$$

The Lyapunov function V is defined based on the squared sliding surface s:

$$V = \frac{1}{2}s^2 \tag{39}$$

For stability, the time derivative of dV/dt must be ≤ 0.

$$\frac{dV}{dt} = s\frac{ds}{dt} = s\left(\sum_{i=1}^{3} k_i \frac{de_i}{dt}\right) \tag{40}$$

Substituting Eq. (39) into Eq. (41), and grouping terms:

$$\frac{dV}{dt} = s\left[k_1\left(\frac{I_{pv}}{C_1} - \frac{\hat{I}_L}{C_1} - \frac{dV_{ref}}{dt}\right) + k_2\left(\frac{V_{pv}}{L} - \frac{\hat{V}_0}{L} - \frac{dI_{L\_ref}}{dt}\right) + k_3\left(\frac{dV_{0\_ref}}{dt} - \frac{\hat{V}_0}{RC_2} - \frac{\hat{I}_L}{C_2}\right) + D\left(\frac{k_3\hat{I}_L}{C_2} + \frac{k_2\hat{V}_0}{L}\right)\right] \tag{41}$$

Substituting the SMC law $u(t) = k_4\text{sign}(s)$ into the expression:

$$\frac{dV}{dt} = s\left[k_1\left(\frac{I_{pv}}{C_1} - \frac{\hat{I}_L}{C_1} - \frac{dV_{ref}}{dt}\right) + k_2\left(\frac{V_{pv}}{L} - \frac{\hat{V}_0}{L} - \frac{dI_{L\_ref}}{dt}\right) + k_3\left(\frac{dV_{0\_ref}}{dt} - \frac{\hat{V}_0}{RC_2} - \frac{\hat{I}_L}{C_2}\right)\right] + k_4\left(\frac{k_3\hat{I}_L}{C_2} + \frac{k_2\hat{V}_0}{L}\right)|s| \tag{42}$$

To ensure stability, dV/dt must be less than zero and must be enforced. By considering the maximum possible values of all physical quantities, e.g., I_{pv_max}, dV_{ref_max}/dt, etc., dV/dt is bounded as follows:

$$\frac{dV}{dt} \leq |s|[Tk_4]_{max} + k_4\left(\frac{k_3\hat{I}_{L\_max}}{C_1} + k_2\frac{\hat{V}_{0\_max}}{L}\right)|s| \tag{43}$$

where T is the terms not containing, to guarantee dV/dt must be less than zero, the maximum magnitude of the non-k_4 terms must be overcome by the k_4 switching term. This leads to conditions on the gains k_i. Therefore, we prove that the two main conditions on the gain k_i are to ensure the negativity of dV/dt. Lower bound on k_1, $\frac{k_1}{C_1} - \frac{k_3}{C_2} > 0$, upper bound on $k_2\frac{dI_{L\_ref_{max}}}{dt} - k_1\frac{I_{pv\_max}}{C_1} > 0$. The global stability condition for the controller gains k_i is expressed by the inequality:

$$\frac{k_3C_1}{C_2} < k_1 < \frac{k_2C_1\dfrac{dI_{L\_ref_{max}}}{dt}}{I_{pv\_max}} \tag{44}$$

By selecting the parameters k_i within this range, it is guaranteed that dV/dt must be less than zero. According to the Lyapunov theory, this mathematically proves the global stability of the system, ensuring that the tracking errors converge to zero and the system effectively tracks the MPPT. The values and parameters for this control method are reused by the author in the study [70].

4. Results and Simulation

A control system for connecting a PV array to the grid has been developed and comprehensively simulated. A comparative analysis is performed to evaluate the performance and efficiency of the proposed control strategy. Specifically, the study focuses on evaluating the robustness and dynamic

response of the controller under two distinct conditions: normal operation and fault conditions. The proposed control system exhibits high stability and reliable performance under all three scenarios, demonstrating its resilience and adaptability to disturbances. The simulation model is constructed in Fig. 1, illustrated Fig. 4 and the control method shown in Fig. 6. During the simulation of the system control using ANN controller under the coordination of SMC and with the participation of ASTO combined called the proposed method, the following parameters are set DC voltage supplied to the rectifier is V_{dc} = 1000 V during the simulation, switching frequency is T_s = 25 ms. Simulation is performed using MATLAB/Simulink [62] to evaluate the performance of the proposed method in MPPT control compared with the conventional control method.

4.1. Case Study 1

The initial analysis of the grid, considering all parameters, was conducted under fault-free conditions in the distribution network, with irradiance levels shown in Fig. 7 and maintained at a constant 25°C. As illustrated in Fig. 8, both the conventional and proposed MPPT control methods ensure stable active power output from the PV array. However, the proposed method demonstrates superior stability throughout the simulation. Consequently, the proposed method maintains a more consistent output power and is less sensitive to variations in irradiance conditions.

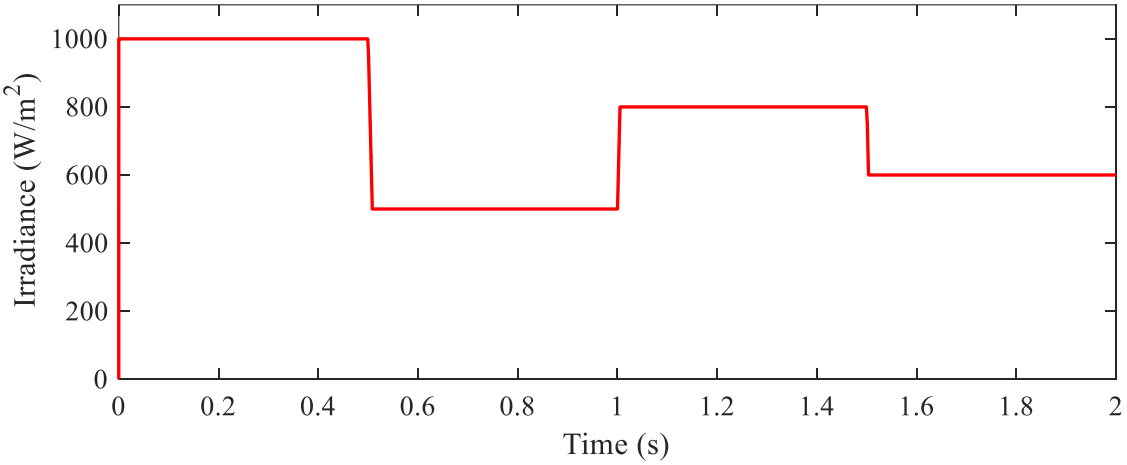

Fig. 7. The solar irradiance pattern applied to PV arrays

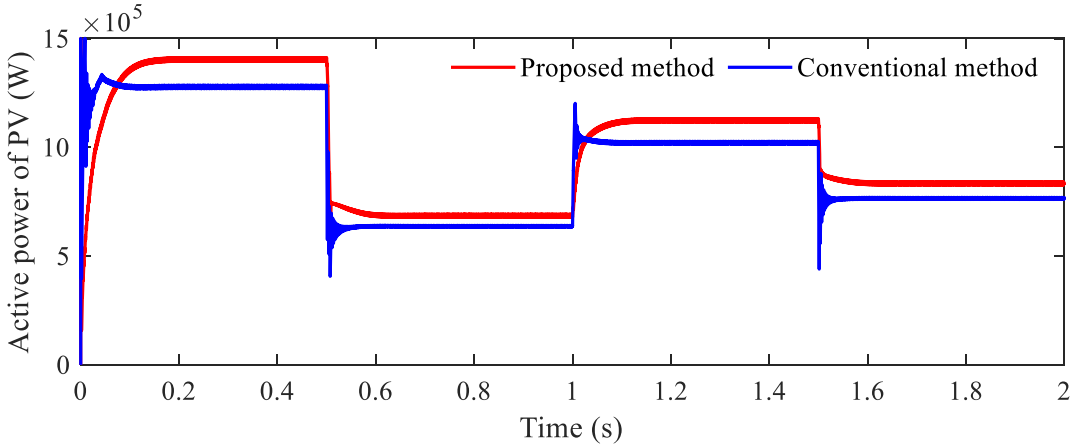

Fig. 8. The active power PV under irradiance levels

Fig. 9 provides a detailed experimental comparison of the performance of the DC link voltage controller under normal operating conditions, contrasting the conventional and proposed methods. Both methods maintain a stable reference voltage of 1,000 V. However, initially, the link voltage for the conventional method rises to about 1,050 V, while the proposed method increases to only around

1,020 V. When transient disturbance events, caused by irradiance fluctuations, occur at various times, the difference in dynamic response becomes evident. The conventional method exhibits a higher overshoot voltage, while the proposed method effectively minimizes this oscillation. During the start-up process, the proposed method reduces the maximum oscillation to approximately 30 V. Though small, this reduction is crucial in minimizing voltage stress on power electronic components, such as capacitors and semiconductors, thereby enhancing the system's reliability and extending its lifespan. Additionally, the proposed method demonstrates faster settling time and better damping, highlighting its superior dynamic response and ability to maintain DC bus stability. In conclusion, these results confirm that the proposed method significantly improves DC link voltage control performance compared to the conventional method.

At 0.5, 1, and 1.5 seconds, the change in irradiance causes the active power to increase from 2.0 MW to approximately 2.75 MW at the initial moment, gradually stabilizing according to the irradiance changes in the subsequent periods, as clearly shown in Fig. 10. In this scenario, the proposed method demonstrates its superiority by exhibiting a significantly faster response time compared to the conventional method, enabling the system to track the new power reference value more efficiently and promptly.

At the same time, Fig. 11 illustrates how the two methods handle reactive power during this state transition. Although the reactive power command remains unchanged, the instantaneous fluctuations in active power still cause crosstalk, resulting in overshoot. Both the conventional and proposed methods maintain improved stability, with the proposed method showing a lower overshoot peak and faster damping of the oscillations. This demonstrates that the proposed method not only enhances the active power response but also improves the control separation between active and reactive power.

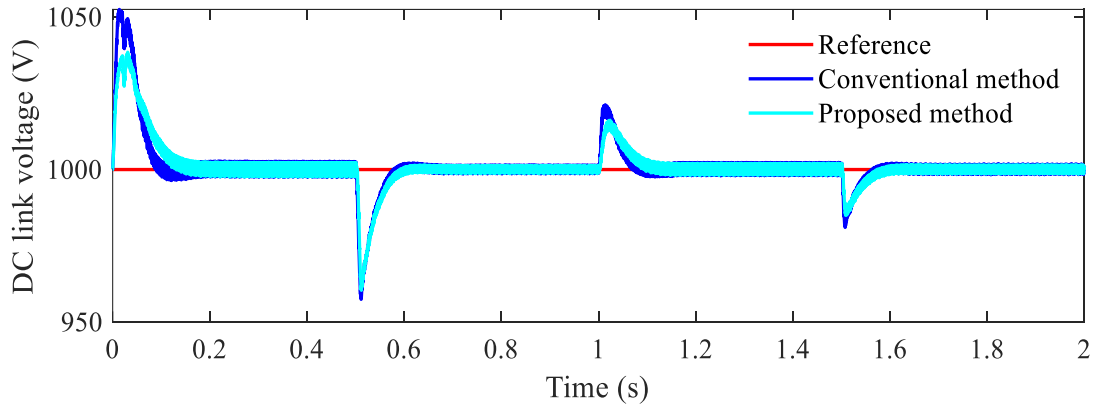

Fig. 9. DC link voltage under irradiance levels

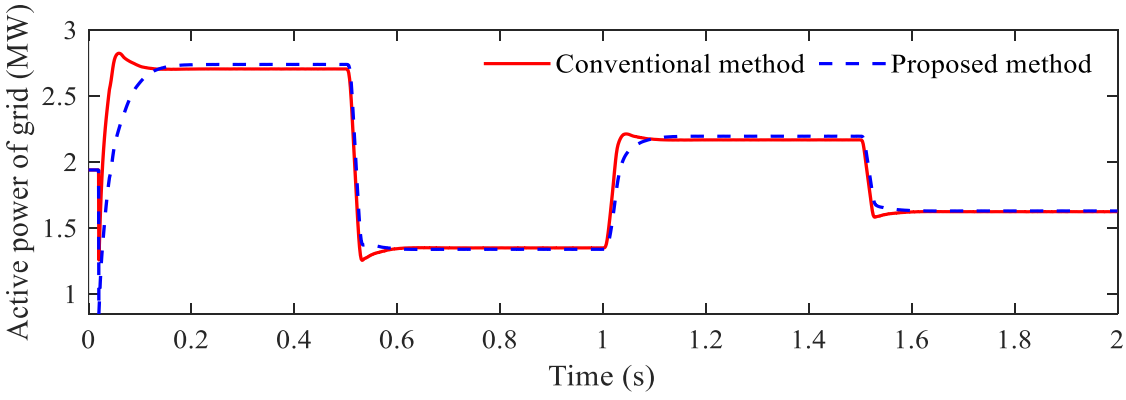

Fig. 10. The active power under irradiance levels

The harmonic analysis of the grid current in phase for both cases, as shown in Fig. 12 and Fig. 13, indicates that both PV inverter configurations deliver grid currents of good quality. The THD

remains low in both cases, measured at 1.39% for the conventional control method and 1.34% for the proposed approach. These values are well within typical power-quality limits, which generally require the current THD to be below 5 percent. A direct comparison shows that the proposed method offers some technical improvements. The THD decreases slightly compared to the traditional scheme, and the amplitude of the fundamental component at 50 Hz is also higher, at 61.85 A compared with 61.75 A. This small increase indicates that the new control strategy enables a more effective transfer of useful power to the grid under the same operating conditions. Overall, although the time-domain waveforms of both methods appear similar, the harmonic spectrum reveals that the proposed method produces a cleaner grid current and improves power-transfer efficiency.

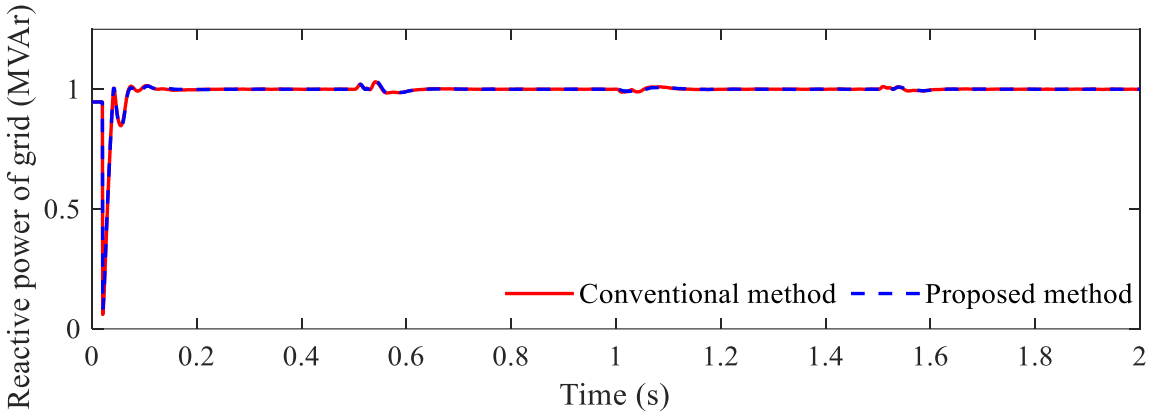

Fig. 11. The reactive power under normal operating conditions

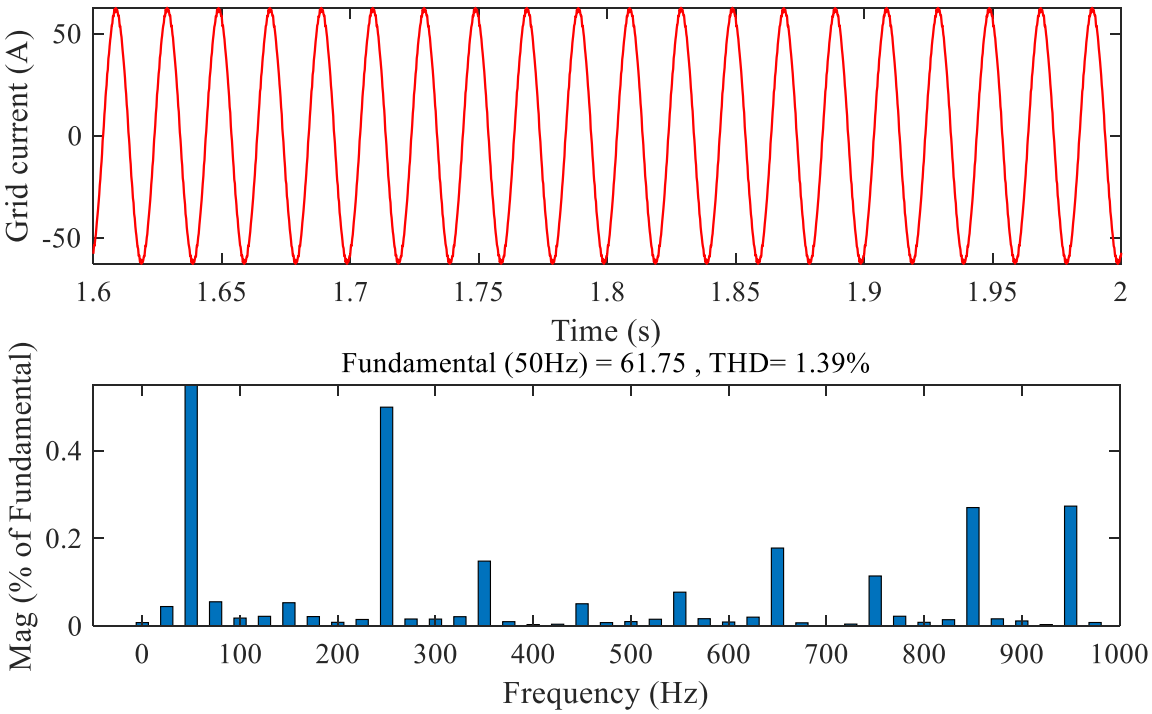

Fig. 12. Harmonic analysis of grid side *a*-phase current by the conventional method in case study 1

4.2. Case Study 2

When assessing the reliability and fault-tolerant capabilities of a grid-connected PV system, two representative fault scenarios are typically analyzed, specifically a symmetrical LLLG and an unsymmetrical single-line-to-ground (LG) fault. The three-phase short circuit is considered the most severe disturbance, as its balanced nature results in the highest fault current, making it ideal for

evaluating protection limits, current withstand capacity, and voltage stability under extreme conditions. In contrast, the single-line-to-ground fault is the most encountered disturbance in practical power networks, introducing voltage and current imbalances that directly impact the PV inverter and power quality at the point of common coupling. Analyzing both fault types provides a comprehensive assessment of the controller's performance and the system's ability to remain stable under both worst-case and commonly occurring grid disturbances, ensuring compliance with modern grid-connection requirements. Subsections 4.2.1 and Subsections 4.2.2, present the asymmetric and symmetric fault scenarios, respectively.

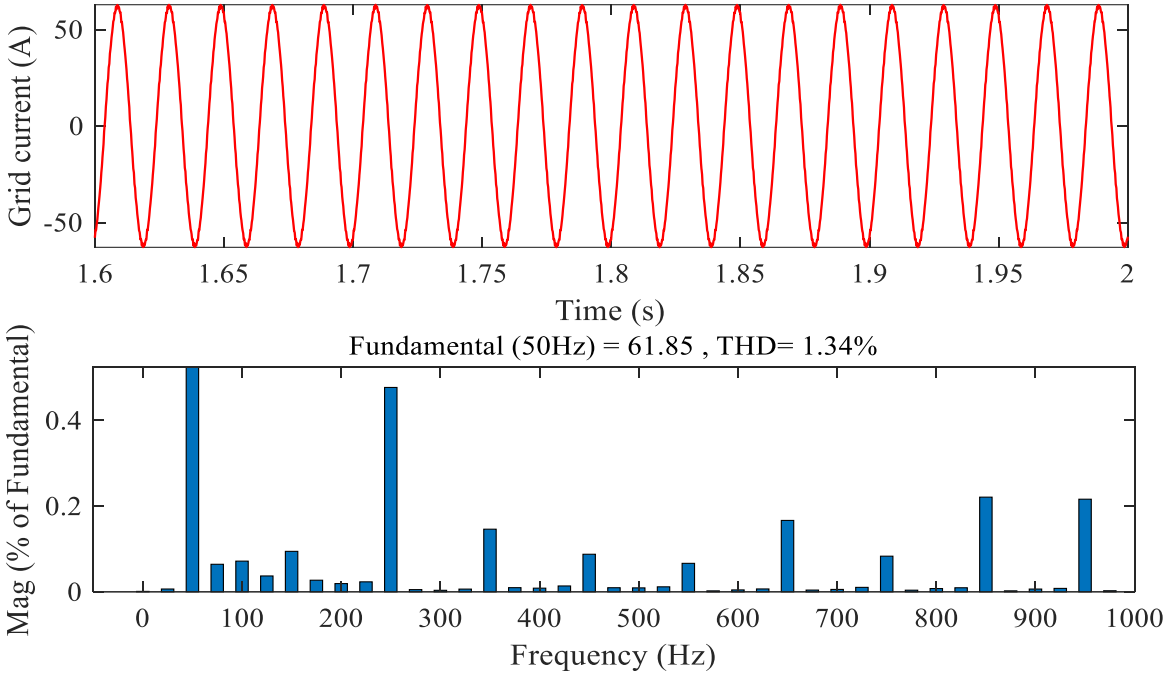

Fig. 13. Harmonic analysis of grid side *a*-phase current using the proposed method in case study 1

4.2.1. Asymmetrical Fault Scenarios

The simulation of the system for the case of an LG fault was conducted at the PCC, as shown in Fig. 4. In this scenario, a short circuit to ground is considered at phase a, with parameters R_{on} = 0.001 Ω, ground resistance R_g = 0.01 Ω, and snubber resistance R_s = 1e6 Ω. The voltage at the PCC for this case is shown in Fig. 14.

This scenario provides a comprehensive evaluation of the robustness and dynamic response of the tested controllers when the PV system is subjected to a LG fault, with a temperature of 25°C and an irradiance of 1000 W/m^2. As shown in Fig. 14, the fault occurs between 0.5 to 0.6 seconds, after which the system is restored to its original value, creating a highly non-linear and challenging environment for maintaining maximum power output. These rapid environmental disturbances allow for an in-depth assessment of how effectively each controller tracks the MPPT while maintaining system stability.

In Fig. 15, the power of the solar panel is shown clearly demonstrating that the proposed method operates more stably and has a faster fault recovery time compared to the conventional method. This indicates that the proposed method has a stronger ability to adjust the amplitude of oscillations, with fault recovery based on values such as voltage, active power, and reactive power, all of which operate more stably and smoothly than in the conventional method.

Fig. 16 illustrates the dynamic response of the grid currents during a single-phase to ground fault. In both cases, the three-phase currents remain balanced before the fault occurs around 0.5 seconds. Once the fault is initiated, the current amplitudes increase sharply and exhibit significant oscillations due to voltage imbalances among the phases. After the fault is cleared for around 0.6 seconds, the

currents rapidly return to their steady-state value. Comparing the two plots reveals that the proposed method achieves faster damping and smoother recovery than the conventional method, showcasing superior capability in maintaining current stability under asymmetrical fault conditions.

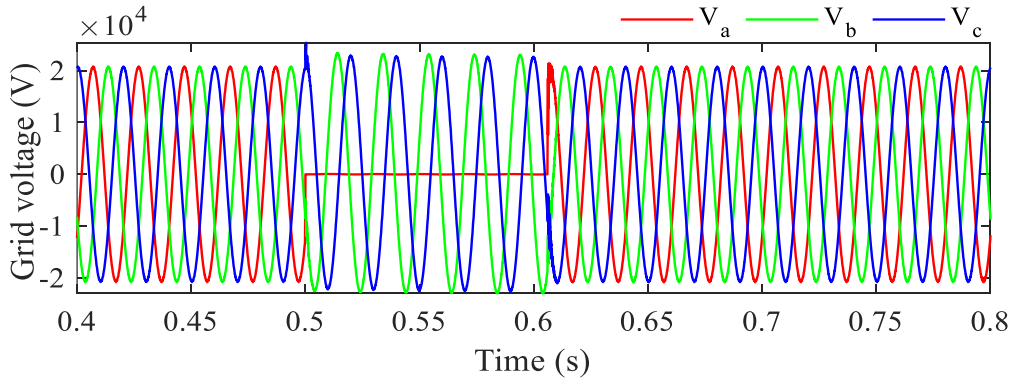

Fig. 14. The three-phase voltage at PCC under LG fault

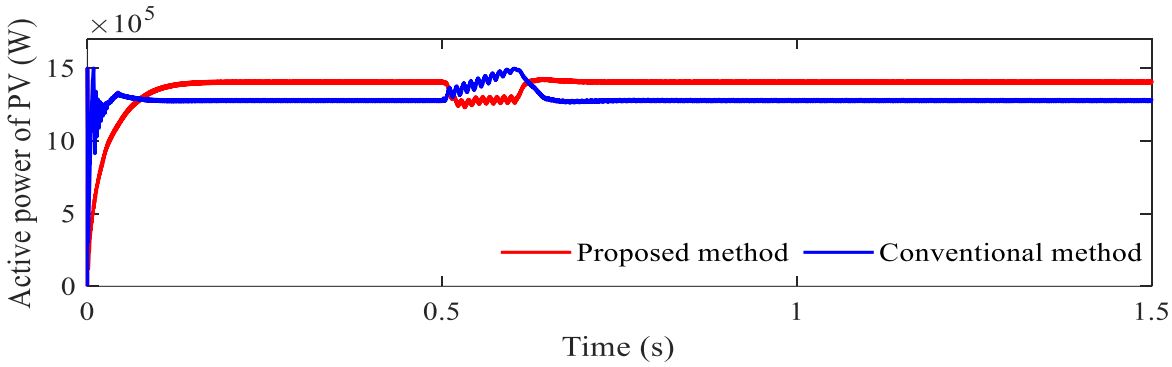

Fig. 15. The output active power of PV under LG fault

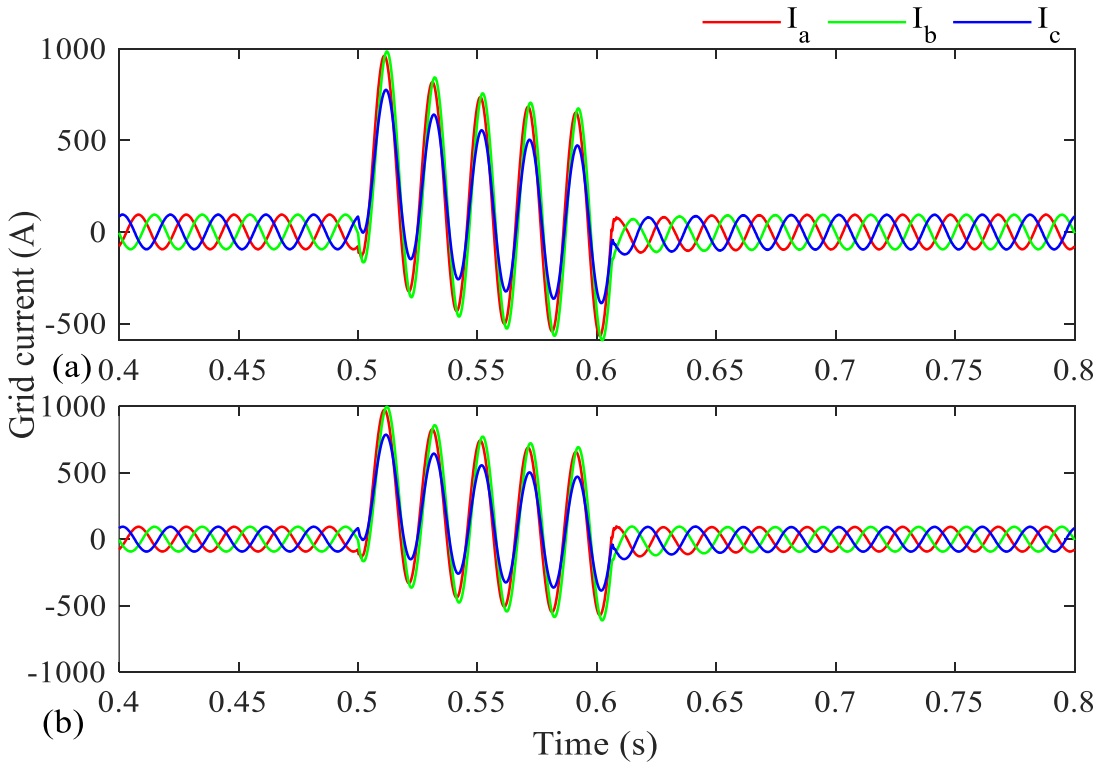

Fig. 16. The grid current under LG fault: (a) the proposed method and (b) the conventional method

Fig. 17 shows the DC link voltage response of the system when a single-phase short circuit fault occurs around 0.5 seconds, with fault recovery occurring after 0.6 seconds. Prior to the fault, the DC link voltage for both methods remains near the reference value of 1,000 V, with the proposed method showing smaller fluctuations. When the fault occurs, the conventional method reacts less stably, as indicated by large amplitude oscillations and voltage spikes reaching up to about 1,000 -1,250 V. In contrast, the proposed method experiences only small oscillations, with a significantly lower voltage increase in the range of 1,000-1,050 V and quickly decreases. The conventional method, however, shows a maximum voltage decrease of about 200 V. After the fault is cleared, the DC link voltage of the proposed method returns to the reference value more quickly and stably, while the conventional method still exhibits residual oscillations. This result demonstrates that the proposed control method is more effective in reducing oscillations and improving the robustness of the DC link voltage under phase-to-earth fault conditions.

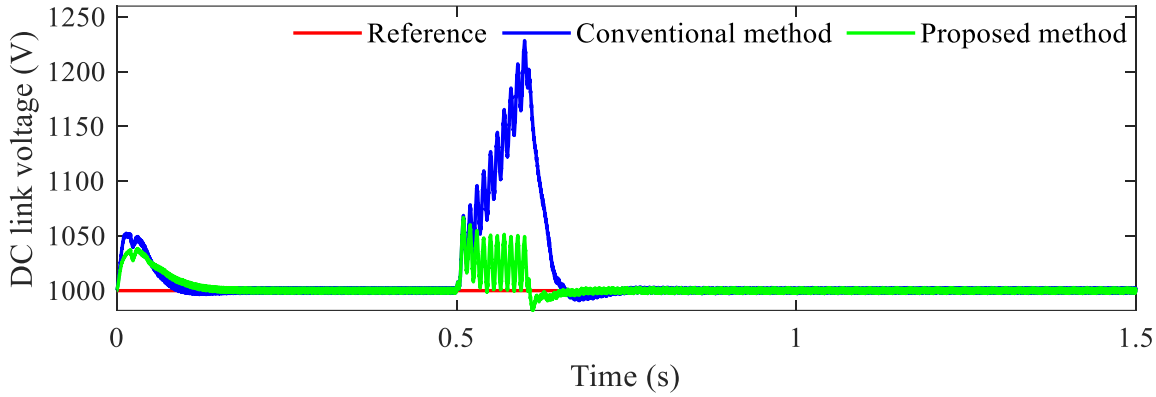

Fig. 17. DC link voltage under LG fault

Fig. 18 illustrates the evolution of the system's active power when an LG fault occurs. Before the fault, both control methods maintain stable active power at approximately 2.75 MW with negligible deviation. However, when the fault occurs at 0.5 seconds, the conventional control method exhibits an unstable response: the active power fluctuates significantly, with a sudden peak that far exceeds the normal operating value. This phenomenon highlights the conventional method's limited ability to manage the power imbalance and voltage fluctuations caused by LG fault. In contrast, the proposed method shows much smaller oscillations, quickly suppresses the disturbance, and restores the active power to a stable value immediately after the fault is cleared. This demonstrates the proposed control strategy's superior robustness to sudden disturbances

Fig. 19 shows the reactive power response under the same fault conditions. Similar to active power, the conventional method again reveals its limitations: the reactive power fluctuates sharply, with many unwanted variations occurring right at the fault time. These fluctuations can negatively impact the voltage condition and stability of the power system. In contrast, the proposed method displays superior control: small reactive fluctuations, rapid stabilization, and smooth retention of the rated state after the fault. This proves that the proposed method is more effective in regulating reactive power exchange, helping to control the voltage more efficiently under adverse conditions.

The simulation results from the three figures clearly demonstrate the superiority of the proposed control method when the system is subjected to a single-phase-to-ground short circuit fault. In all three critical quantities DC-link voltage in Fig. 17, active power in Fig. 18, and reactive power in Fig. 19, the conventional method shows significant limitations, including large fluctuations, transient surges, and long recovery times after the fault. These characteristics highlight the conventional method's weak anti-disturbance capabilities and dynamic instability under asymmetric grid conditions. In contrast, the proposed control method outperforms the conventional method across all three indicators. In every case, it maintains a lower oscillation amplitude, significantly reduces overshoot, and restores steady-state conditions more quickly after the fault is cleared. For DC-link voltage, the proposed method effectively limits voltage surges and rapidly returns the value to the reference level. For both active

and reactive power, the proposed controller minimizes power disturbances at the fault instant and maintains stability during the post-fault process. This demonstrates better coordination between system components and high adaptability to short-term disturbances. Overall, the simulation results from all three figures clearly show that the proposed control method offers significantly higher robustness, damping ability, and control quality compared to the conventional method. This confirms the potential application of the proposed method in renewable energy systems and power converters operating in grid environments with frequent disturbances and adverse conditions.

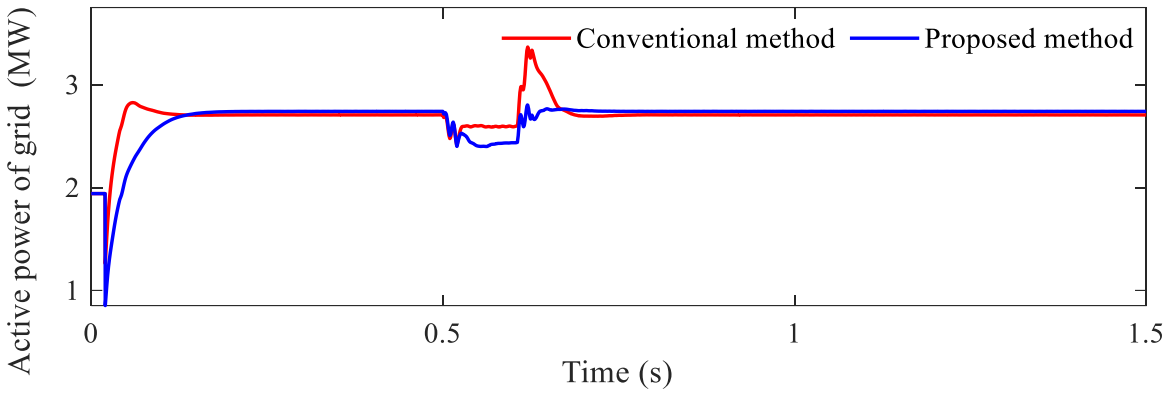

Fig. 18. The active power under LG fault

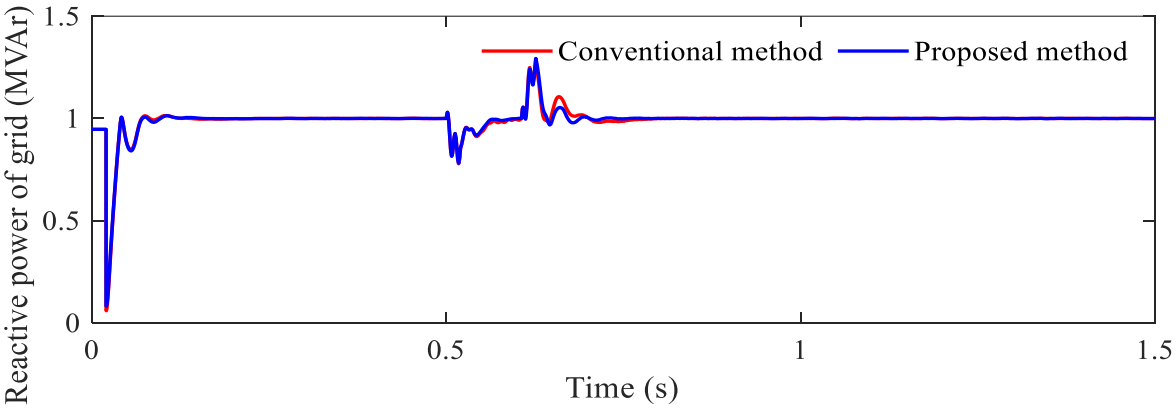

Fig. 19. The reactive power under LG fault

An examination of Fig. 20 and Fig. 21, which correspond to a large transient current event likely caused by a grid voltage sag, highlights the critical role of the PV inverter controller in disturbance rejection. Both control methods demonstrate grid-fault ride-through capability by injecting a high reactive current during the disturbance and restoring stable operation once the event has passed. However, in the post-fault steady state, the proposed method shows a clear performance advantage in terms of power quality and power transfer efficiency. The proposed method achieves a THD of 1.78%, which is lower than the 1.95% obtained with the conventional method. This reduction indicates improved stability and better harmonic compensation under high-power operating conditions. Furthermore, the fundamental current component reaches 93.94 A, which is 1.55 A higher than that of the conventional method. This improvement confirms that the new control algorithm enhances the extraction and delivery of useful power to the grid, which is particularly important after grid-disturbance events.

4.2.2. Symmetrical Fault Scenarios

Next, the simulation system for the LLLG fault is performed at the PCC, as shown in Fig. 4. In this case, a short circuit to ground occurs across all three phases a, b, and c with updated parameters including R_{on} = 1 Ω, ground resistance R_g = 0.01 Ω, and snubber resistance R_s = 1e6 Ω. The voltage at the PCC in this scenario is shown in Fig. 23. This scenario provides a comprehensive evaluation of

the robustness and dynamic response of the tested controllers when the PV system is subjected to an LLLG fault, with a temperature of 25°C and varying irradiance, as shown in Fig. 22. Simultaneously, the DC link voltage is adjusted to 1050 V over a period of 1 to 1.5 seconds, as seen in Fig. 26.

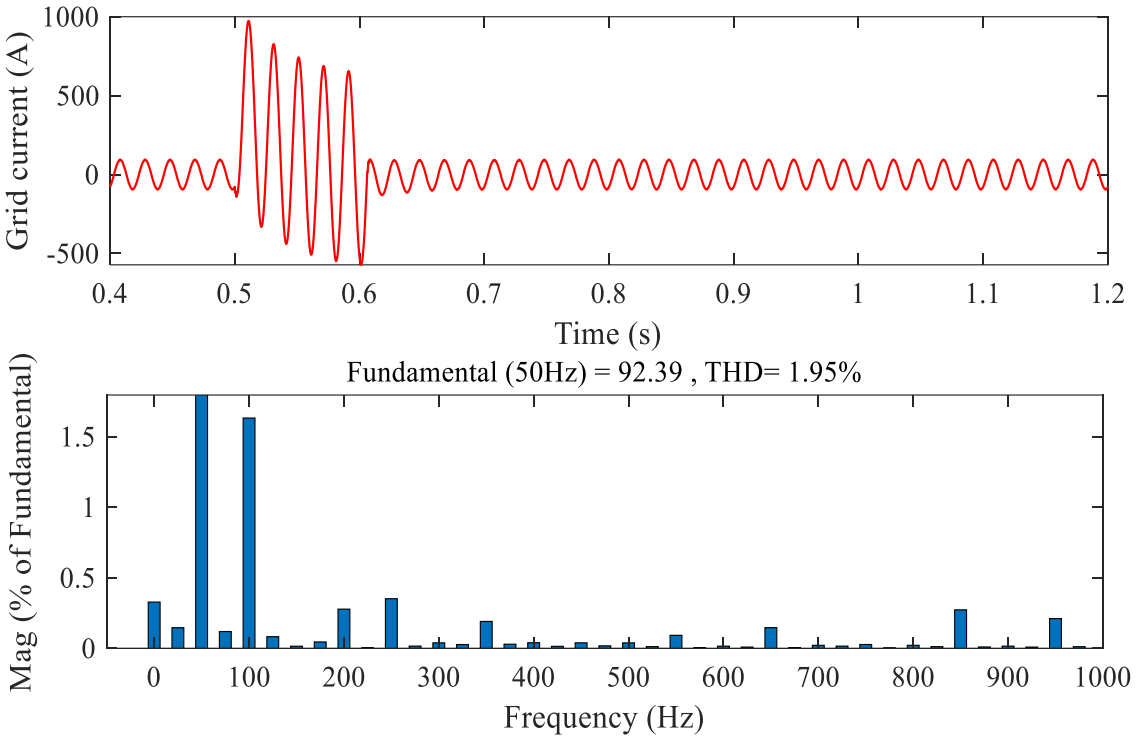

Fig. 20. Harmonic analysis of grid side *a*-phase current by the conventional method under LG fault

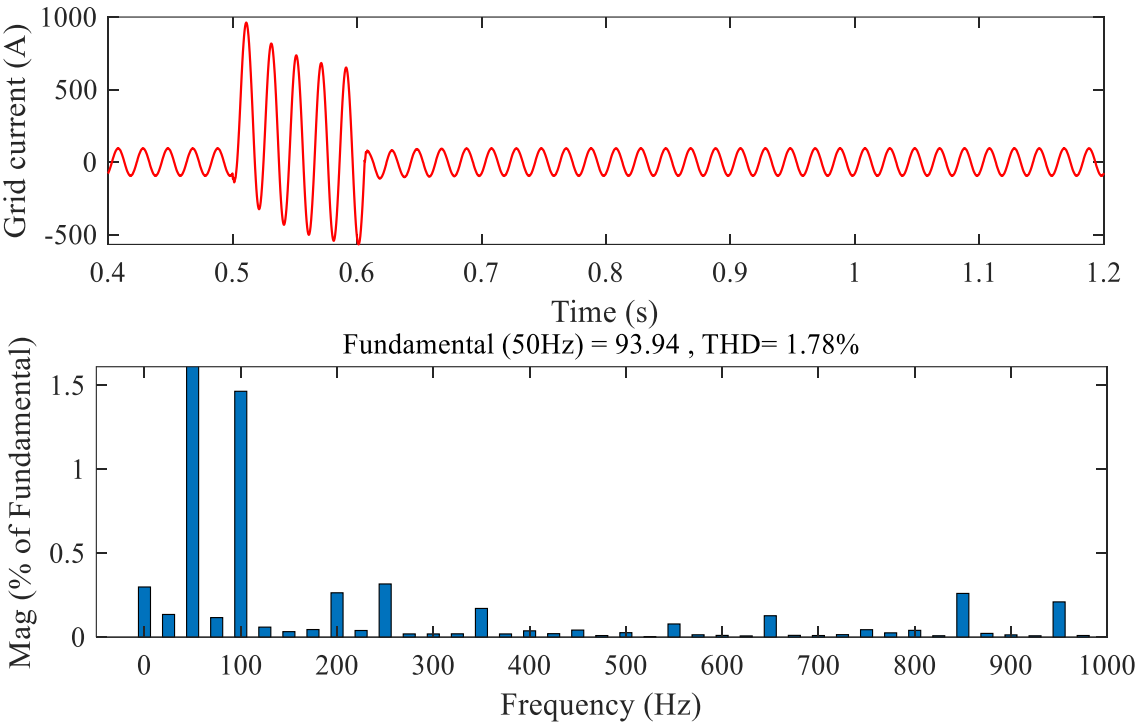

Fig. 21. Harmonic analysis of grid side *a*-phase current by the proposed method under LG fault

Analysis Fig. 24, which shows the dynamic behavior of the grid current during a severe LLLG fault, confirms that the proposed method offers superior stability and safety compared to the

conventional method. When the fault occurs around 1.2 seconds, both control strategies provide the current required to support the grid as part of the undervoltage overshoot response. However, once the fault is cleared around 1.3 seconds, the difference between the two methods becomes clear. The proposed method enables smooth and rapid grid voltage recovery, successfully limiting the peak transient current to around 500 A, as shown in Fig. 24 (a). In contrast, the conventional method results in much higher transient currents, exceeding 600 A, as shown in Fig. 24 (b), along with a less stable grid voltage recovery. This behavior is directly linked to the improved DC voltage regulation capability of the proposed method, as shown earlier in Fig. 26, which enables more precise operation of the grid current control loop. This reduces stress on power electronic components and ensures compliance with the grid's dynamic recovery requirements after a fault.

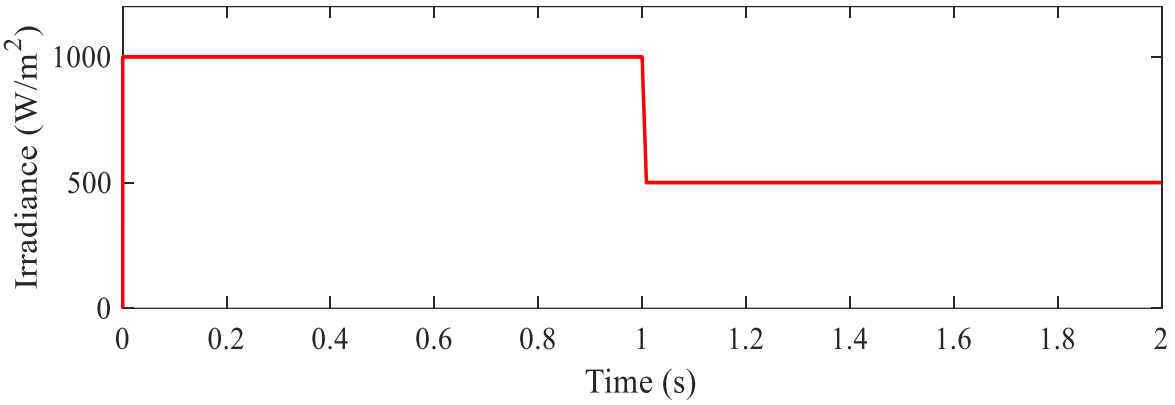

Fig. 22. The solar irradiance pattern applied to PV arrays

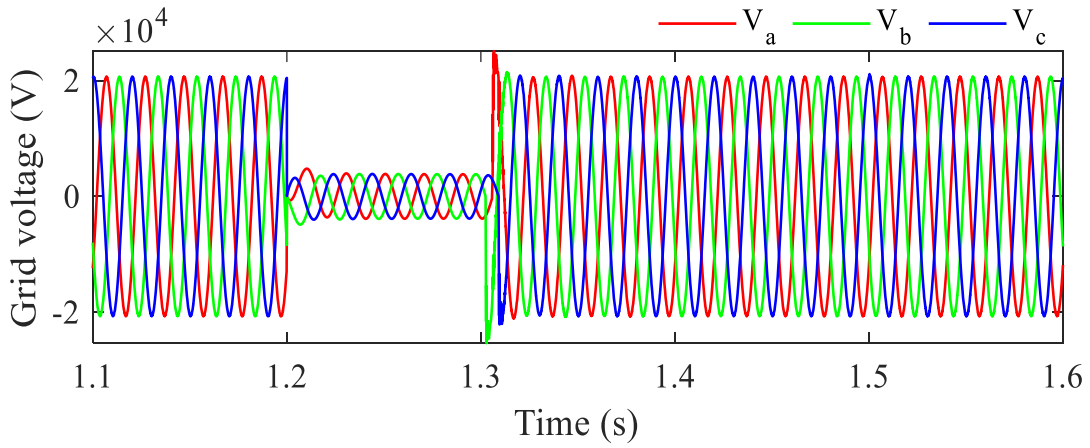

Fig. 23. The three-phase at PCC under LLLG fault

Fig. 25 illustrates the dynamic response of the PV power when the system is subjected to a sudden change in solar irradiance while simultaneously experiencing a grid disturbance. During the initial period of constant irradiance from 0 to 1 second, both the proposed method and the conventional method effectively track the MPPT. However, after 1 second, when the irradiance decreases and the new DC-link voltage reference is applied, the power obtained using the proposed method shows noticeable oscillations and a deeper transient drop compared to the conventional method, particularly between 1.2 and 1.4 seconds. Although both methods eventually converge with the new MPPT, these fluctuations suggest that under complex transient conditions, the MPPT tracking performance of the proposed method may be more sensitive to rapid changes in the DC-link voltage.

Fig. 26 provides clear evidence of the controllers' robustness when the system is subjected to both a simultaneous LLLG fault and a step change in the DC voltage reference to 1,050 V between 1 and 1.5 seconds. The proposed method demonstrates a highly stable response, efficiently raising and

regulating the DC-link voltage to 1050 V with minimal overshoot. In contrast, the conventional method fails to maintain stability, resulting in a severe DC-voltage spike approaching 1,800 V. This excessive overshoot exceeds the design safety limits and could cause physical damage to power devices and DC-link capacitors. Therefore, Fig. 26 confirms that the proposed method offers superior disturbance rejection and stronger DC-voltage loop stability, ensuring safe and reliable inverter operation under severe grid-fault conditions.

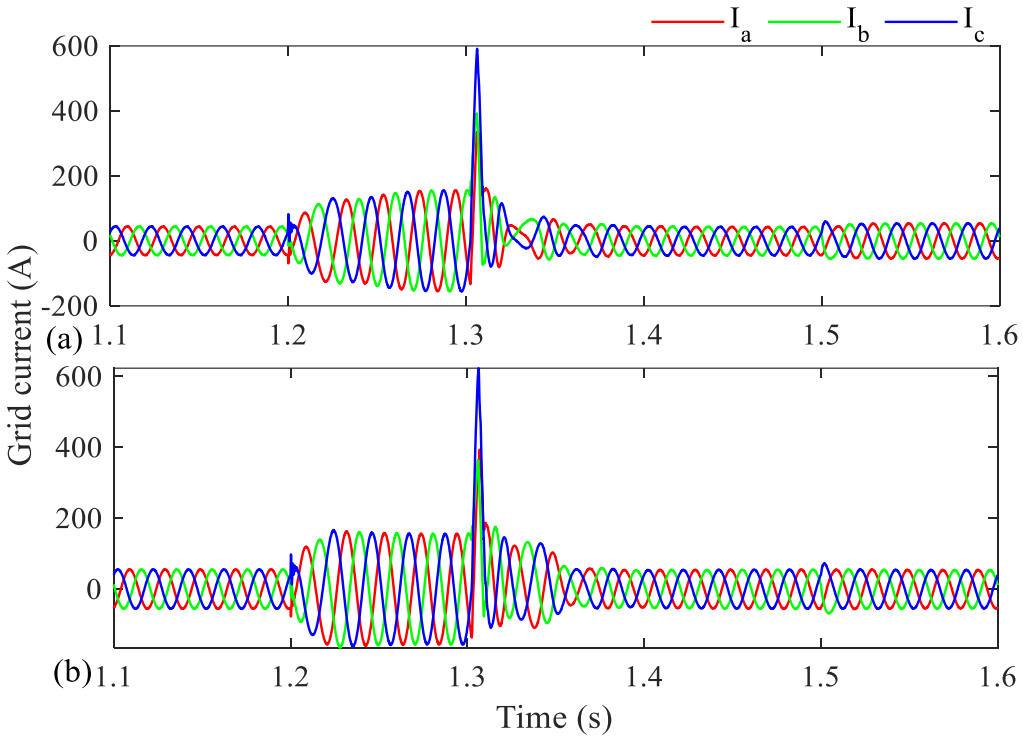

Fig. 24. The grid current under LLLG fault: (a) the proposed method and (b) the conventional method

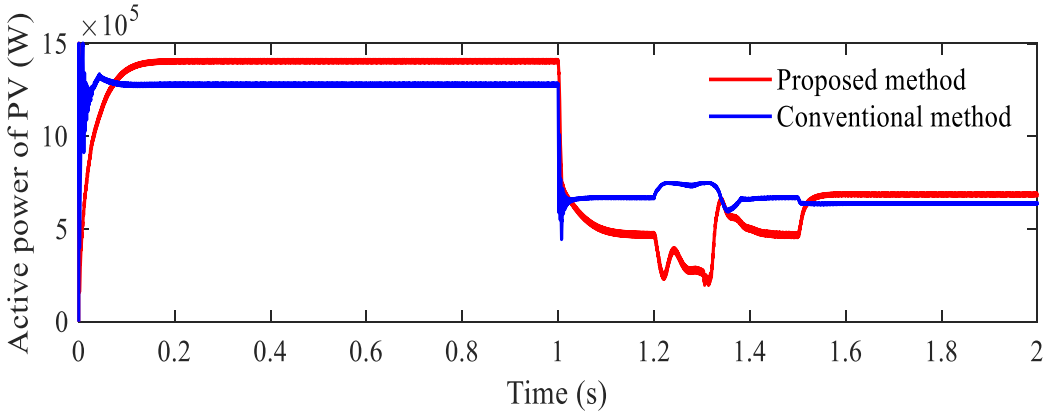

Fig. 25. The output active power of PV under LLLG fault

Fig. 27 and Fig. 28 illustrate the qualitative differences between the conventional and proposed methods in controlling active and reactive power when the PV system experiences a severe grid fault, along with changing operating conditions. In Fig. 25, during the grid-fault interval from approximately 1.2 to 1.3 seconds, the conventional method fails to maintain stable operation, evident from a sharp drop in active power followed by an uncontrolled rise that exceeds 3 MW once the fault is cleared. This overshoot is a direct result of the loss of DC-link voltage regulation, as shown earlier in Fig. 26. The resulting instability in the DC-link voltage leads to saturation and loss of coordination in the current-control loop, causing the inverter to inject excessive power into the grid. In contrast, the

proposed method maintains tight control over the active power response. The power recovers smoothly and quickly to the new MPPT, which is lower due to the reduced irradiance, after approximately 1.4 seconds. This stable dynamic recovery demonstrates that the proposed method incorporates a more effective anti-windup mechanism and better coordination between the control loops, ensuring reliable power regulation during and after severe grid disturbances.

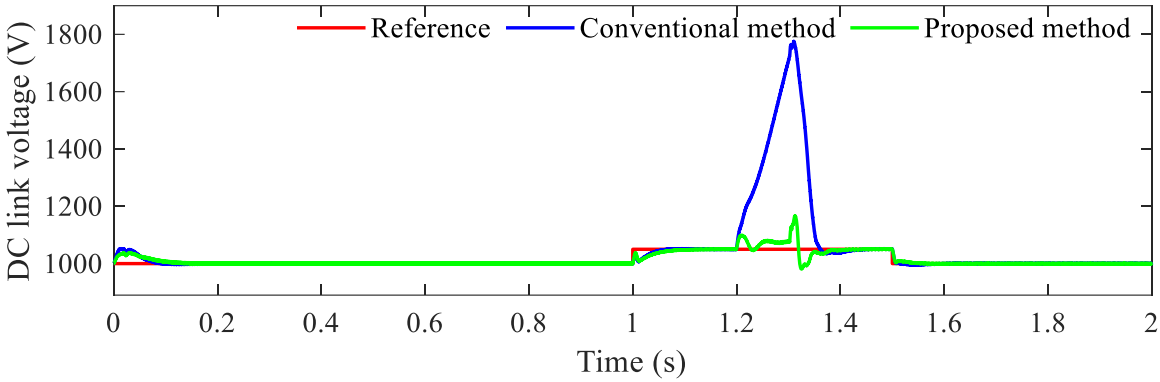

Fig. 26. DC link voltage under LLLG fault

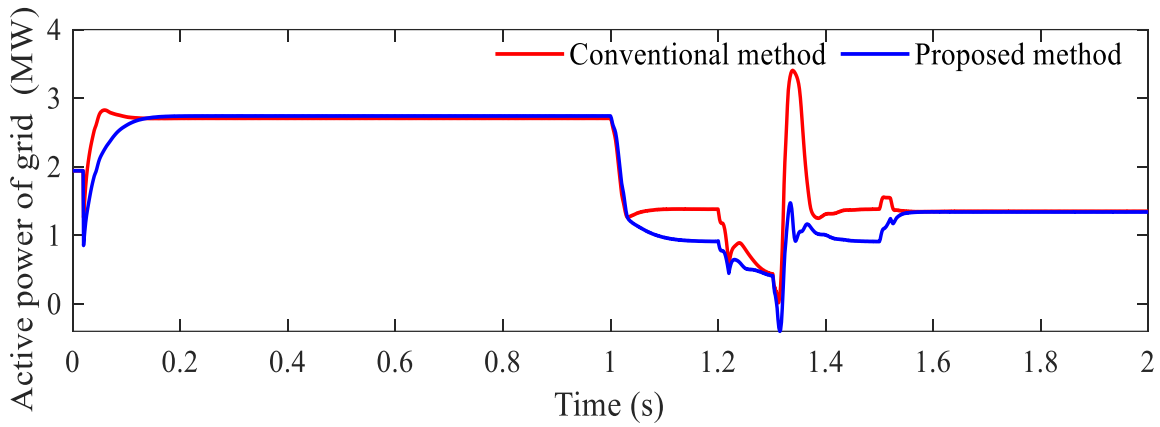

Fig. 27. The active power under LLLG fault

According to low-voltage ride-through requirements, both control methods inject positive reactive power into the grid during the voltage sag to support the grid voltage. However, at the moment of voltage recovery around 1.3 seconds, the conventional method exhibits instability by producing a large transient peak, reaching nearly 3 MVAr. Such a sudden spike is undesirable, as it can introduce voltage oscillations and place unnecessary stress on the grid. In contrast, the proposed method keeps the reactive power response well-controlled, with a significantly smaller transient peak and a rapid return to the reference level of 1 MVAr. This difference indicates that the proposed method regulates the reactive current component more accurately, reducing disturbances and ensuring strict compliance with power quality and post-fault grid support requirements. Therefore, Fig. 27 and Fig. 28 demonstrate the practical robustness of the proposed method, showing that it maintains stable delivery of both active and reactive power under harsh operating conditions an important advantage over the conventional method.

A harmonic analysis of the grid-side phase-a current, following the severe conditions of the symmetrical fault scenario, reveals a clear improvement in power quality when using the proposed method, as shown in Fig. 29 and Fig. 30. The proposed method achieves a lower THD of 1.47%, compared to 1.51% with the conventional method, indicating its ability to maintain a cleaner current waveform even after a grid fault and a significant DC-voltage disturbance. Although the fundamental current component of the proposed method is slightly reduced, measuring 53.94 A compared to 54.35 A with the conventional method, this small decrease represents a reasonable trade-off for the enhanced

dynamic stability and disturbance rejection provided by the controller. The reduction in THD demonstrates that the proposed method improves the effectiveness of the current-control loop, minimizes low-order harmonic content, and ensures compliance with stringent grid power-quality requirements across all operating conditions.

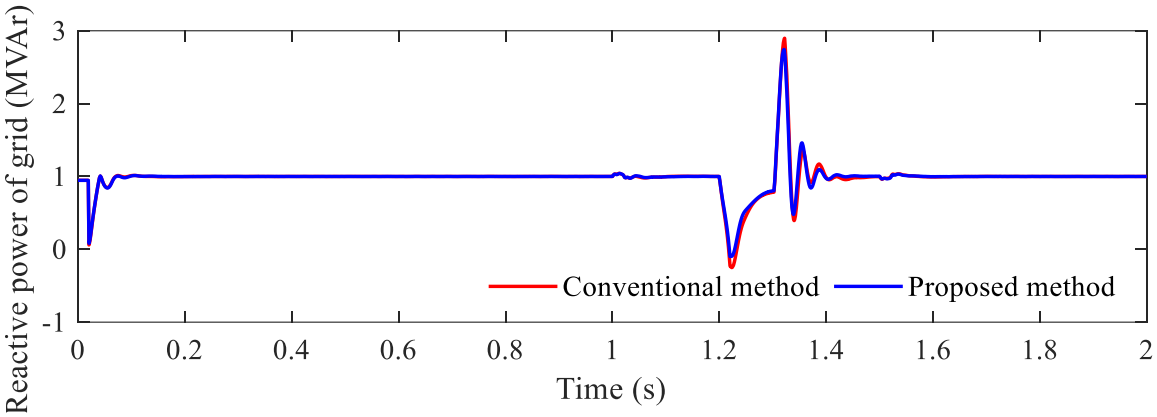

Fig. 28. The reactive power under LLLG fault

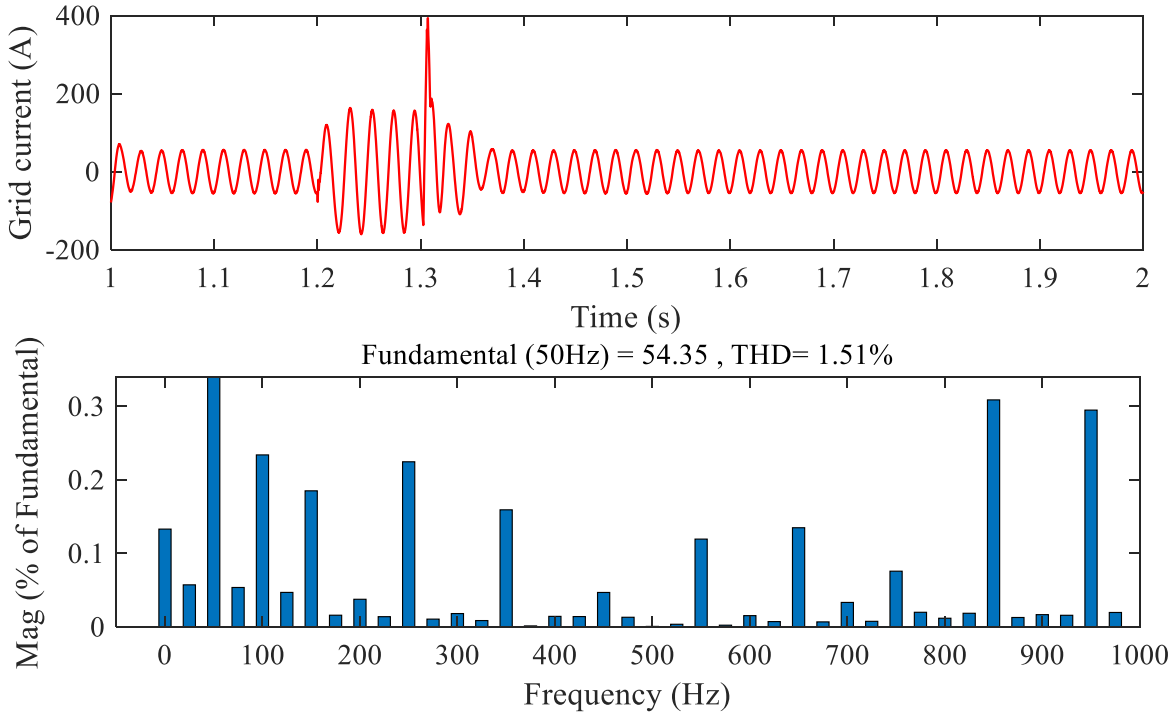

Fig. 29. Harmonic analysis of *a*-phase grid current under LLLG fault applying the conventional method

Fig. 31 presents a comparison of the fundamental component amplitude at 50 Hz and the THD of the phase current across the three studied scenarios, comparing the conventional and proposed methods. The results show that the THD of the proposed method is consistently lower in all two cases, demonstrating its ability to maintain more stable power quality, particularly when the system is subjected to adverse operating conditions in symmetrical fault scenarios. The amplitude of the fundamental component of the proposed method also shows less variation, reflecting a more robust current control characteristic and a reduced impact from DC voltage fluctuations. This confirms that the proposed method enhances the efficiency of the current control loop and limits the energy of low-order harmonic components. These results indicate that the new algorithm is better suited for grid-connected PV applications, where maintaining low THD and waveform stability across a wide range of operating conditions is essential.

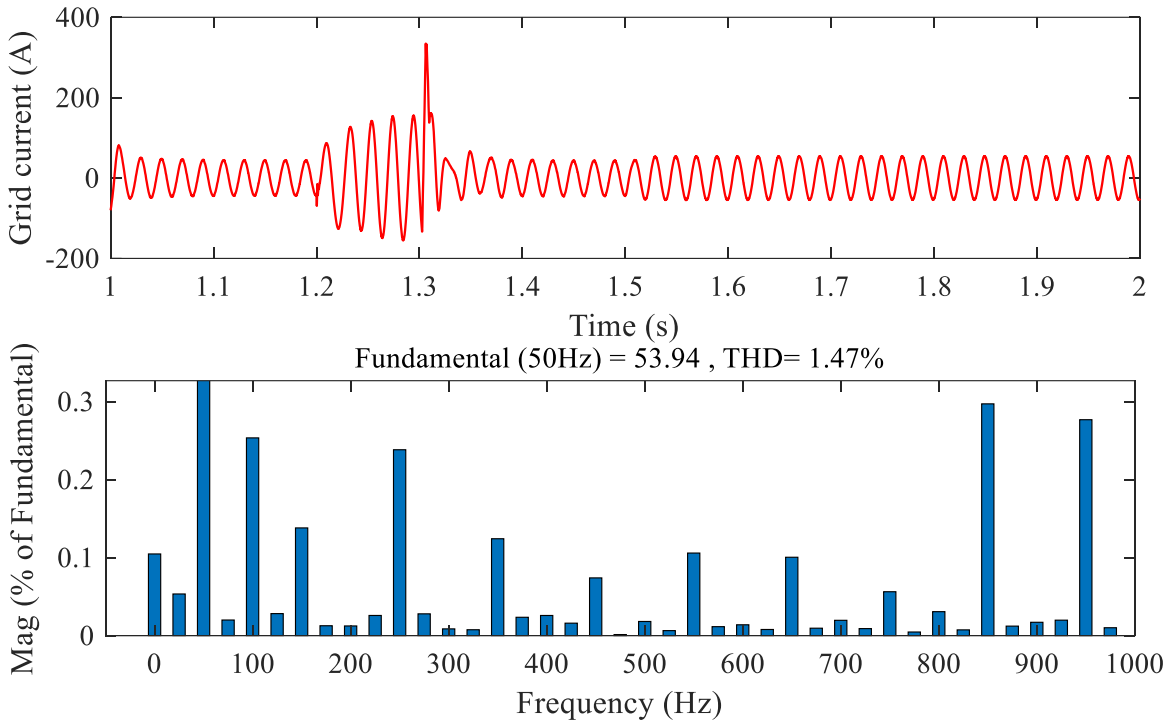

Fig. 30. Harmonic analysis of a-phase grid current under LLLG fault applying the proposed method

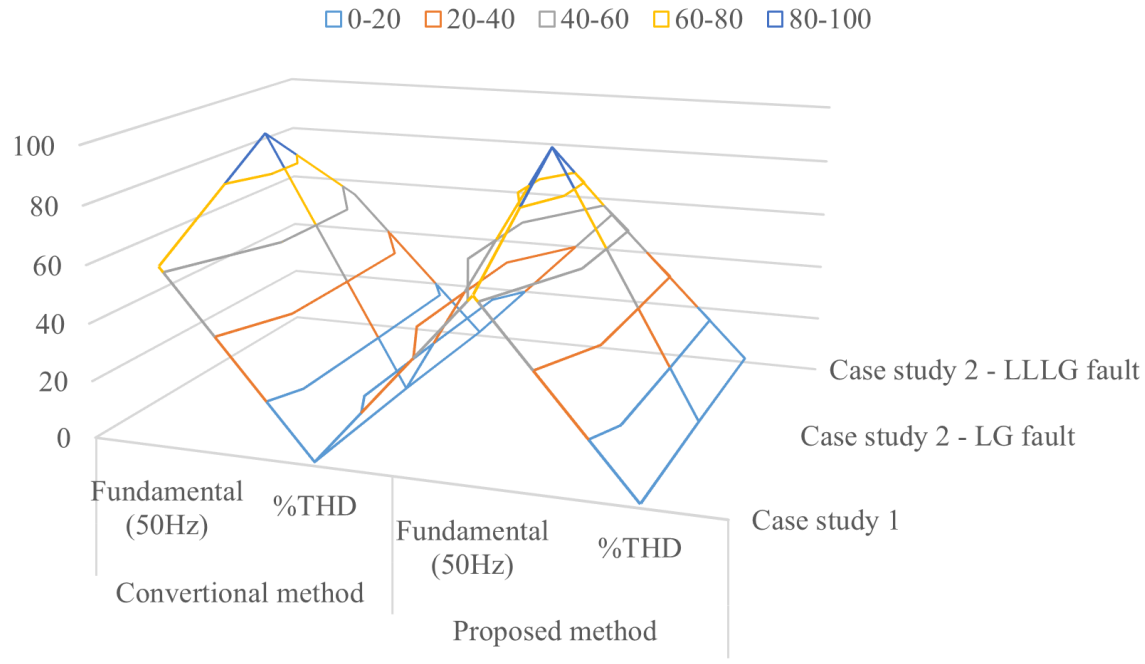

Fig. 31. Comparison of the fundamental components and THD values of phase-*a* currents in three studied cases by the conventional and proposed methods

5. Conclusion

This study successfully addresses the challenge of enhancing stability and power quality in grid-connected photovoltaic (PV) systems by designing and implementing a novel adaptive hybrid control strategy. By integrating an artificial neural network (ANN) for optimal reference generation with sliding mode control (SMC) and an adaptive super-twisting observer (ASTO), the research overcomes the limitations of conventional methods, such as slow convergence and high sensitivity to

disturbances. The simulation results, validated under various operating conditions, lead to the following specific conclusion:

1) Enhanced tracking performance and stability under normal operations: The proposed controller demonstrates superior dynamic response under rapidly changing irradiance, reducing the DC-link voltage overshoot to approximately 20 V, compared to 50 V with the conventional method. Additionally, the grid's current quality is improved, as indicated by a reduction in total harmonic distortion (THD) from 1.39% to 1.34%. This confirms that the ANN-based feed-forward mechanism provides precise maximum power point (MPP) estimation, while the ASTO effectively minimizes the chattering phenomenon inherent in SMC, ensuring smoother steady-state operation.

2) Robustness against asymmetrical grid faults: Under single-line-to-ground fault conditions, the proposed method demonstrates significant fault-tolerant capability, limiting the DC-link voltage surge to 1050 V, while the conventional method experiences a spike up to 1250 V. The system also achieves a low current THD of 1.78%, compared to 1.95% in the conventional method. This improved resilience is attributed to the observer's ability to accurately estimate and compensate for unbalanced grid voltages in real-time, preventing destabilization of the control loop during the transient phase.

3) Superior fault ride-through during severe symmetrical faults: In the critical scenario of a three-phase -to-ground fault combined with DC-link voltage step changes, the proposed strategy proves its value by maintaining the DC voltage near the 1050 V reference, effectively eliminating the dangerous 1800 V spike observed with the conventional approach. Furthermore, peak transient currents are limited to approximately 500 A, compared to over 600 A with the conventional method. This distinct advantage results from the robust nonlinear nature of the SMC law, which, unlike linear controllers, maintains stability even during grid voltage collapse, thereby protecting power electronic components from electrical stress.

Author Contribution: All authors contributed equally to the main contributor to this paper. All authors read and approved the final paper.

Funding: Please add: This research received no external funding

Acknowledgment: The authors would like to thank the managers and the members of the "*International Journal of Robotics and Control Systems*" for their valuable comments and suggestions.

Conflicts of Interest: The authors declare no conflict of interest.

References

[1] C. Nagarajan, B. Tharani, S. Saravanan, and R. Prakash, "Performance estimation and control analysis of AC-DC/DC-DC hybrid multi-port intelligent controllers based power flow optimizing using STEM strategy and RPFC technique," *International Journal of Robotics and Control Systems*, vol. 2, no. 1, pp. 124-139, 2022, https://doi.org/10.31763/ijrcs.v2i1.562.

[2] M. S. Endiz, G. Gökkuş, A. E. Coşgun, and H. Demir, "A review of traditional and advanced MPPT approaches for PV systems under uniformly insolation and partially shaded conditions," *Applied Sciences*, vol. 15, no. 3, p. 1031, 2025, https://doi.org/10.3390/app15031031.

[3] R. Asghar *et al*., "Wind energy potential in Pakistan: A feasibility study in Sindh province," *Energies*, vol. 15, no. 22, p. 8333, 2022, https://doi.org/10.3390/en15228333.

[4] M. Y. Worku *et al*., "A comprehensive review of recent maximum power point tracking techniques for photovoltaic systems under partial shading," *Sustainability*, vol. 15, no. 14, p. 11132, 2023, https://doi.org/10.3390/su151411132.

[5] B. T. H. Phuong, T. T. Ngoc, P. H. Thanh, and L. Van Dai, "Mitigating Subsynchronous Resonance in Doubly Fed Wind Turbine Induction Generator Using FACTS Devices: A Comparative Case Study,"

International Journal of Robotics and Control Systems, vol. 5, no. 1, pp. 311-332, 2025, https://doi.org/10.31763/ijrcs.v5i1.1436.

[6] Z. Reguieg, I. Bouyakoub, F. Mehedi, and F. Bouhadji, "Optimizing Power Quality: Simulation of UPQC Integrated PV with Comprehensive Reliability and Performance Analysis," *International Journal of Smart Grid-ijSmartGrid*, vol. 8, no. 1, pp. 46-52, 2024, https://doi.org/10.20508/ijsmartgrid.v8i1.333.g338.

[7] A. N. Mahmood *et al*., "Experimental Analysis of Fresnel Lens-Based Solar Desalination Systems with Copper Receivers for Enhanced Thermal and Electrical Performance," *International Journal of Robotics & Control Systems*, vol. 5, no. 2, pp. 1191-1210, 2025, https://doi.org/10.31763/ijrcs.v5i2.1852.

[8] H. M. Bawayan, M. A. Enany, M. M. Elymany, A. A. Shaier, and M. M. Ahmed, "Control strategies of hybrid RESs for off-grid water pumping technologies: An overview," *Scientific African*, vol. 29, p. e02856, 2025, https://doi.org/10.1016/j.sciaf.2025.e02856.

[9] T. A. Almalaisi *et al*., "Optimization of Harmonic Elimination in PV-Fed Asymmetric Multilevel Inverters Using Evolutionary Algorithms," *International Journal of Robotics & Control Systems*, vol. 5, no. 2, pp. 902-916, 2025, https://dx.doi.org/10.31763/ijrcs.v5i2.1785.

[10] V. T. K. Nhi, B. T. Quy, H. H. B. Nghia, and L. V. Dai, "A Robust Hybrid Control Strategy for Enhancing Torque Stability and Performance in PMSM Drives," *Electrical Engineering & Electromechanics*, no. 6, pp. 64-74, 2025, https://doi.org/10.20998/2074-272X.2025.6.09.

[11] U. Hussan *et al*., "Robust Maximum Power Point Tracking in PV Generation System: A Hybrid ANN-Backstepping Approach With PSO-GA Optimization," *IEEE Transactions on Consumer Electronics*, vol. 71, no. 2, pp. 6016-6026, 2025, https://doi.org/10.1109/TCE.2025.3569871.

[12] B. M. Bellah, B. Tahar, and B. Adel, "Adaptive hybrid MPPT using artificial intelligence for an autonomous PV system," *International Journal of Smart Grid-ijSmartGrid*, vol. 8, no. 1, pp. 27-34, 2024, https://doi.org/10.20508/ijsmartgrid.v8i1.328.g331.

[13] Y. Duan, Y. Zhao, and J. Hu, "An initialization-free distributed algorithm for dynamic economic dispatch problems in microgrid: Modeling, optimization and analysis," *Sustainable Energy, Grids and Networks*, vol. 34, p. 101004, 2023, https://doi.org/10.1016/j.segan.2023.101004.

[14] P. Li, J. Hu, L. Qiu, Y. Zhao, and B. K. Ghosh, "A distributed economic dispatch strategy for power–water networks," *IEEE Transactions on Control of Network Systems*, vol. 9, no. 1, pp. 356-366, 2021, https://doi.org/10.1109/tcns.2021.3104103.

[15] M. J. Nahar, M. R. Sarkar, M. Uddin, M. F. Hossain, M. M. Rana, and M. R. Tanshen, "Single axis solar tracker for maximizing power production and sunlight overlapping removal on the sensors of tracker," *International Journal of Robotics and Control Systems*, vol. 1, no. 2, pp. 186-197, 2021, https://doi.org/10.31763/ijrcs.v1i2.333.

[16] N. Deghfel, A. E. Badoud, F. Merahi, M. Bajaj, and I. Zaitsev, "A new intelligently optimized model reference adaptive controller using GA and WOA-based MPPT techniques for photovoltaic systems," *Scientific Reports*, vol. 14, no. 1, p. 6827, 2024, https://doi.org/10.1038/s41598-024-57610-0.

[17] E. Mohammadi, M. Alizadeh, M. Asgarimoghaddam, X. Wang, and M. G. Simões, "A review on application of artificial intelligence techniques in microgrids," *IEEE Journal of Emerging and Selected Topics in Industrial Electronics*, vol. 3, no. 4, pp. 878-890, 2022, https://doi.org/10.1109/JESTIE.2022.3198504.

[18] T. T. Nguyen, T. D. Pham, L. C. Kien, and L. Van Dai, "Improved coyote optimization algorithm for optimally installing solar photovoltaic distribution generation units in radial distribution power systems," *Complexity*, vol. 2020, no. 1, p. 1603802, 2020, https://doi.org/10.1155/2020/1603802.

[19] C. Keo, S. Srang, and R. Seng, "Performance Investigation of Low-Cost Dual-Axis Solar Tracker using Light Dependent Resistor," *International Journal of Robotics & Control Systems*, vol. 3, no. 4, pp. 853-869, 2023, https://doi.org/10.31763/ijrcs.v3i4.1137.

[20] N. Cherigui, A. Chemidi, A. Tahour, and M. Horch, "A new advanced third-order sliding mode control with adaptive gain adjustment using fuzzy logic technique for standalone photovoltaic systems," *AIMS*

Electronics and Electrical Engineering, vol. 9, no. 2, pp. 243-259, 2025, https://doi.org/10.3934/electreng.2025012.

[21] H. M. H. Farh, A. Fathy, A. A. Al-Shamma'a, S. Mekhilef, and A. M. Al-Shaalan, "Global research trends on photovoltaic maximum power extraction: Systematic and scientometric analysis," *Sustainable Energy Technologies and Assessments*, vol. 61, p. 103585, 2024, https://doi.org/10.1016/j.seta.2023.103585.

[22] C. H. H. Basha, T. Naresh, K. Amaresh, P. Preethi Raj, and P. Akram, "Design and performance analysis of common duty ratio controlled zeta converter with an adaptive P&O MPPT controller," *Proceedings of International Conference on Data Science and Applications: ICDSA 2021*, vol. 1, pp. 657-671, 2021, https://doi.org/10.1007/978-981-16-5120-5_50.

[23] A. Belkaid, K. Kayisli, ILHAMI COLAK, Slimane HADJI, Ouahib GUENOUNOU, "Smart Power Conditioning Unit Utilizing Enhanced Inc-Con MPPT for Photovoltaic Power Plants," *International Journal of Smart Grid-ijSmartGrid*, vol. 8, no. 1, pp. 41-45, 2024, https://doi.org/10.20508/ijsmartgrid.v8i1.330.g335.

[24] A. H. Hamed, A.-N. Sharkawy, I. Hamdan, and H. M. Maghrabie, "Automated Water Cooling and Solar Tracking for Efficiency Improvement of PV Systems: A Systematic Review," *International Journal of Robotics and Control Systems*, vol. 4, no. 4, pp. 1819-1861, 2024, https://doi.org/10.31763/ijrcs.v4i4.1642.

[25] E.-C. Chang, C.-A. Cheng, and L.-S. Yang, "Nonsingular terminal sliding mode control based on binary particle swarm optimization for DC–AC converters," *Energies*, vol. 12, no. 11, p. 2099, 2019, https://doi.org/10.3390/en12112099.

[26] A. Cabrera-Tobar, E. Bullich-Massagué, M. Aragüés-Peñalba, and O. Gomis-Bellmunt, "Topologies for large scale photovoltaic power plants," *Renewable and Sustainable Energy Reviews*, vol. 59, pp. 309-319, 2016, https://doi.org/10.1016/j.rser.2015.12.362.

[27] S. Sobri, S. Koohi-Kamali, and N. A. Rahim, "Solar photovoltaic generation forecasting methods: A review," *Energy conversion and management*, vol. 156, pp. 459-497, 2018, https://doi.org/10.1016/j.enconman.2017.11.019.

[28] K. Ullah, M. Ishaq, F. Tchier, H. Ahmad, and Z. Ahmad, "Fuzzy-based maximum power point tracking (MPPT) control system for photovoltaic power generation system," *Results in Engineering*, vol. 20, p. 101466, 2023, https://doi.org/10.1016/j.rineng.2023.101466.

[29] M. Mahdi, M. S. Rahal, M. Taha, R. Nuwayhid, G. Abou Haidar, and R. Achkar, "Smart Hybrid Inverter Design Using Simulink and Solar Assistant," *International Journal of Smart Grid-ijSmartGrid*, vol. 8, no. 2, pp. 108-114, 2024, https://doi.org/10.20508/ijsmartgrid.v8i2.343.g353.

[30] A.-N. Sharkawy, M. M. Ali, H. H. Mousa, A. S. Ali, and G. Abdel-Jaber, "Short-term solar PV power generation day-ahead forecasting using artificial neural network: Assessment and validation," *International Journal of Robotics and Control Systems*, vol. 2, no. 3, pp. 562-580, 2022, https://doi.org/10.31763/ijrcs.v2i3.780.

[31] A. Modi, F. Bühler, J. G. Andreasen, and F. Haglind, "A review of solar energy based heat and power generation systems," *Renewable and Sustainable Energy Reviews*, vol. 67, pp. 1047-1064, 2017, https://doi.org/10.1016/j.rser.2016.09.075.

[32] T. Bahi and A. Lakhdara, "Analysis of Genetic and Cuckoo Search Algorithms for MPPT in Partial Shaded," *International Journal of Smart Grid-ijSmartGrid*, vol. 8, no. 1, pp. 35-40, 2024, https://doi.org/10.20508/ijsmartgrid.v8i1.329.g330.

[33] J. S. Saputro, H. Maghfiroh, F. Adriyanto, M. R. Darmawan, M. H. Ibrahim, and S. Pramono, "Energy Monitoring and control of automatic transfer switch between grid and solar panel for home system," *International Journal of Robotics and Control Systems*, vol. 3, no. 1, pp. 59-73, 2023, https://doi.org/10.31763/ijrcs.v3i1.843.

[34] Y. L. Chuang, M. Herrera, and A. Balal, "Using PV fuzzy tracking algorithm to charge electric vehicles," *International Journal of Robotics and Control Systems*, vol. 2, no. 2, pp. 253-261, 2022, https://doi.org/10.31763/ijrcs.v2i2.636.

[35] N. V. T. Kieu, N. H. H. Bao, and T. Q. Bach, "A Model Advanced Predictive Current Control Strategy for PMSM Drives with Torque Ripple and Current Harmonic Reduction," *Journal of Robotics and Control (JRC)*, vol. 6, no. 5, pp. 2444-2456, 2025, https://doi.org/10.18196/jrc.v6i5.26908.

[36] P. Pourmaleki, W. Agutu, A. Rezaei, and N. Pourmaleki, "Techno-economic analysis of a 12-kW photovoltaic system using an efficient multiple linear regression model prediction," *International Journal of Robotics and Control Systems*, vol. 2, no. 2, pp. 370-378, 2022, https://doi.org/10.31763/ijrcs.v2i2.702.

[37] B. E. Elnaghi, A. M. Ismaiel, M. M. Ismail, H. A. Zedan, and A. A. Salem, "Experimental validation of an adaptive fuzzy logic controller for MPPT of grid connected PV system," *Scientific Reports*, vol. 15, no. 1, p. 27173, 2025, https://doi.org/10.1038/s41598-025-10188-7.

[38] F. Belhachat and C. Larbes, "Comprehensive review on global maximum power point tracking techniques for PV systems subjected to partial shading conditions," *Solar Energy*, vol. 183, pp. 476-500, 2019, https://doi.org/10.1016/j.solener.2019.03.045.

[39] B. Yang *et al*., "Comprehensive overview of maximum power point tracking algorithms of PV systems under partial shading condition," *Journal of Cleaner Production*, vol. 268, p. 121983, 2020, https://doi.org/10.1016/j.jclepro.2020.121983.

[40] M. H. Zafar, N. M. Khan, A. F. Mirza, and M. Mansoor, "Bio-inspired optimization algorithms based maximum power point tracking technique for photovoltaic systems under partial shading and complex partial shading conditions," *Journal of Cleaner Production*, vol. 309, p. 127279, 2021, https://doi.org/10.1016/j.jclepro.2021.127279.

[41] M. Uoya and H. Koizumi, "A calculation method of photovoltaic array's operating point for MPPT evaluation based on one-dimensional Newton–Raphson method," *IEEE Transactions on Industry Applications*, vol. 51, no. 1, pp. 567-575, 2014, https://doi.org/10.1109/tia.2014.2326083.

[42] M. Killi and S. Samanta, "Modified perturb and observe MPPT algorithm for drift avoidance in photovoltaic systems," *IEEE transactions on Industrial Electronics*, vol. 62, no. 9, pp. 5549-5559, 2015, https://doi.org/10.1109/tie.2015.2407854.

[43] L. Shang, H. Guo, and W. Zhu, "An improved MPPT control strategy based on incremental conductance algorithm," *Protection and Control of Modern Power Systems*, vol. 5, no. 2, pp. 1-8, 2020, https://doi.org/10.1186/s41601-020-00161-z.

[44] A. G. Abo-Khalil, I. I. El-Sharkawy, A. Radwan, and S. Memon, "Influence of a hybrid MPPT technique, SA-P&O, on PV system performance under partial shading conditions," *Energies*, vol. 16, no. 2, p. 577, 2023, https://doi.org/10.3390/en16020577.

[45] Y. Xiao, Y. Zhao, Z. Shen, and H. Jiao, "SMGSA algorithm-based MPPT control strategy," *Journal of Power Electronics*, vol. 24, no. 5, pp. 789-798, 2024, https://doi.org/10.1007/s43236-023-00757-2.

[46] A. Harrag and S. Messalti, "Variable step size modified P&O MPPT algorithm using GA-based hybrid offline/online PID controller," *Renewable and Sustainable Energy Reviews*, vol. 49, pp. 1247-1260, 2015, https://doi.org/10.1016/j.rser.2015.05.003.

[47] N. Chaibakhsh, M. B. A. Rahman, F. Vahabzadeh, S. Abd-Aziz, M. Basri, and A. B. Salleh, "Optimization of operational conditions for adipate ester synthesis in a stirred tank reactor," *Biotechnology and Bioprocess Engineering*, vol. 15, no. 5, pp. 846-853, 2010, https://doi.org/10.1007/s12257-010-0001-7.

[48] L. Wang, H. Liu, L. V. Dai, and Y. Liu, "Novel method for identifying fault location of mixed lines," *Energies*, vol. 11, no. 6, p. 1529, 2018, https://doi.org/10.3390/en11061529.

[49] A. Chellakhi and S. El Beid, "Principle and Simulation Investigation of The Newly Proposed MPPT Approaches," *Optimizing Solar Photovoltaic Systems*, pp. 93-150, 2025, https://doi.org/10.1007/978-3-031-93283-0_4.

[50] M. Alkahtani, Z. Wu, C. S. Kuka, M. S. Alahammad, and K. Ni, "A Novel PV array reconfiguration algorithm approach to optimising power generation across non-uniformly aged PV arrays by merely repositioning," *J*, vol. 3, no. 1, p. 5, 2020, https://doi.org/10.3390/j3010005.

[51] H. Rizki, F. E.-z. Lamzouri, E.-M. Boufounas, A. El Amrani, and L. Bejjit, "Advanced global MPPT strategy for PV systems using high-order sliding mode control, ABC optimization, and neural network

prediction under partial shading conditions," *Computers and Electrical Engineering*, vol. 127, p. 110562, 2025, https://doi.org/10.1016/j.compeleceng.2025.110562.

[52] K. Kavin, P. S. Karuvelam, M. Matcha, and S. Vendoti, "Improved BRBFNN-based MPPT algorithm for coupled inductor KSK converter for sustainable PV system applications," *Electrical Engineering*, pp. 1-23, 2025, https://doi.org/10.1007/s00202-025-02952-9.

[53] B. U. D. Abdullah, S. L. Dhar, S. P. Jaiswal, M. M. Gulzar, M. Alqahtani, and M. Khalid, "Hybrid MPPT control using hybrid pelican optimization algorithm with perturb and observe for PV connected grid," *Frontiers in Energy Research*, vol. 12, p. 1505419, 2025, https://doi.org/10.3389/fenrg.2024.1505419.

[54] N. Rishikesh and J. S. Kumar, "Integrated PV energy generation system with high-gain converter and CHHO-FLC-based MPPT for grid integration," *Electrical Engineering*, vol. 107, no. 4, pp. 4873-4896, 2025, https://doi.org/10.1007/s00202-024-02791-0.

[55] N. Hannan, M. A. Rahman Akash, A. Shufian, A. K. Roy, M. S. Ashraf and R. Islam, "A Comparative Analysis of PSO and ANN Based MPPT for Power Optimization with In-Depth Performance Assessment in Residential PV On-Grid Solar Systems," *2025 IEEE Region 10 Symposium (TENSYMP)*, pp. 1-8, 2025, https://doi.org/10.1109/tensymp63728.2025.11144944.

[56] A.-M. Badea, D. Manaila-Maximean, L. Fara, and D. Craciunescu, "Maximizing solar photovoltaic energy efficiency: MPPT techniques investigation based on shading effects," *Solar Energy*, vol. 285, p. 113082, 2025, https://doi.org/10.1016/j.solener.2024.113082.

[57] N. Hannan, M. A. Rahman Akash, A. Shufian, A. K. Roy, M. S. Ashraf and R. Islam, "A Comparative Analysis of PSO and ANN Based MPPT for Power Optimization with In-Depth Performance Assessment in Residential PV On-Grid Solar Systems," *2025 IEEE Region 10 Symposium (TENSYMP)*, pp. 1-8, 2025, https://doi.org/10.1109/TENSYMP63728.2025.11144944.

[58] A. Belkaid, S. HADJI, and L. Larbi, "Modified Topology of SEPIC Converter with High Gain Transfer Ratio for PV Applications," *International Journal of Smart Grid-ijSmartGrid*, vol. 8, no. 4, pp. 199-204, 2024, https://doi.org/10.20508/ijsmartgrid.v8i4.363.g368.

[59] P. H. Thanh and L. V. Dai, "A Reliable Tool Based on the Fuzzy Logic Control Method Applying to the DC/DC Boost Converter of Off-Grid Photovoltaic to Track the Maximum Power Point," *International Journal of Intelligent Systems and Applications in Engineering*, vol. 11, pp. 831-843, 2023, https://ijisae.org/index.php/IJISAE/article/view/3616.

[60] B. Dhouib, M. A. Zdiri, Z. Alaas, and H. Hadj Abdallah, "Fault analysis of a small PV/wind farm hybrid system connected to the grid," *Applied Sciences*, vol. 13, no. 3, p. 1743, 2023, https://doi.org/10.3390/app13031743.

[61] O. I. Okieh, S. Seker, T. C. Akinci, and A. I. Idriss, "Optimization of Neuro-controller Application for Maximum Power Point Tracking Photovoltaic Systems Through Shannon's Information Criteria," *Electric Power Components and Systems*, pp. 1-12, 2024, https://doi.org/10.1080/15325008.2024.2328799.

[62] B. Naima *et al*., "Enhancing MPPT optimization with hybrid predictive control and adaptive P&O for better efficiency and power quality in PV systems," *Scientific Reports*, vol. 15, no. 1, p. 24559, 2025, https://doi.org/10.1038/s41598-025-10335-0.

[63] M. Y. Dennai and H. Tedjini, "Integrating hybrid artificial ecosystem with P&O MPPT for enhanced fuel cell performance in microgrid systems," *Electrical Engineering*, vol. 107, pp. 8059-8084, 2025, https://doi.org/10.1007/s00202-025-02962-7.

[64] S. M. Hadi, "Enhancing Power Tracking Efficiency in Stand-Alone PV Systems via Adaptive Perturb and Observe (P&O) Optimization," *Journal of University of Babylon for Engineering Sciences*, vol. 33, no. 3, pp. 100-117, 2025, https://doi.org/10.29196/jubes.v33i3.5760.

[65] M. W. Lotfy and A. I. Hussein, "Power Extraction in Photovoltaic Systems using P&O-Based MPPT with DC-DC Buck Converter Integration," *WSEAS Transactions on Electronics*, vol. 16, pp. 51-59, 2025, https://doi.org/10.37394/232017.2025.16.6.

[66] B. Fatna, D. Yousfi and A. Rahmouni, "Optimization of Photovoltaic Systems Under Partial Shading: A Comparative Analysis of PSO and P&O Algorithms," *2025 International Conference on Circuit, Systems and Communication (ICCSC)*, pp. 1-7, 2025, https://doi.org/10.1109/ICCSC66714.2025.11135125.

[67] D. Nishad, A. Tiwari, S. Khalid, S. Gupta, and A. Shukla, "AI-based hybrid power quality control system for electrical railway using single phase PV-UPQC with Lyapunov optimization," *Scientific Reports*, vol. 15, no. 1, p. 2641, 2025, https://doi.org/10.1038/s41598-025-85393-5.

[68] A. Demirci, I. Dagal, S. Mirza Tercan, H. Gundogdu, M. Terkes and U. Cali, "Enhanced ANN-Based MPPT for Photovoltaic Systems: Integrating Metaheuristic and Analytical Algorithms for Optimal Performance Under Partial Shading," *IEEE Access*, vol. 13, pp. 92783-92799, 2025, https://doi.org/10.1109/access.2025.3572554.

[69] D. Salman, Y. K. Elmi, A. M. Isak, and A. Sheikh-Muse, "Evaluation of MPPT Algorithms for Solar PV Systems with Machine Learning and Metaheuristic Techniques," *Mathematical Modelling of Engineering Problems*, vol. 12, no. 1, pp. 115-124, 2025, https://doi.org/10.18280/mmep.120113.

[70] H. Abidi, L. Sidhom, M. Bollen, and I. Chihi, "Adaptive software sensor for intelligent control in photovoltaic system optimization," *International Journal of Electrical Power & Energy Systems*, vol. 170, p. 110921, 2025, https://doi.org/10.1016/j.ijepes.2025.110921.

[71] L. Sidhom, I. Chihi, and E. N. Kamavuako, "Software sensor to enhance online parametric identification for nonlinear closed-loop systems for robotic applications," *Sensors*, vol. 21, no. 11, p. 3653, 2021, https://doi.org/10.3390/s21113653.

[72] A. K. Pati and N. C. Sahoo, "A super-twisting sliding mode observer for boost inverter-based hybrid photovoltaic-battery system control," *Transactions of the Institute of Measurement and Control*, vol. 42, no. 12, pp. 2139-2154, 2020, https://doi.org/10.1177/0142331220906964.

[73] R. B. Roy *et al*., "A Comparative Performance Analysis of ANN Algorithms for MPPT Energy Harvesting in Solar PV System," *IEEE Access*, vol. 9, pp. 102137-102152, 2021, https://doi.org/10.1109/ACCESS.2021.3096864.

[74] H. Abidi, L. Sidhom and I. Chihi, "Innovative Hybrid Intelligent Robust MPPT for PV Systems in Dynamic Environments," *2023 14th International Renewable Energy Congress (IREC)*, pp. 1-6, 2023, https://doi.org/10.1109/IREC59750.2023.10389450.